Restoration of DNA Integrity and Cell Cycle by Electric Stimulation in Planarian Tissues Damaged by Ionizing Radiation

Devon Davidian[1,2,#], Melanie LeGro[1,2,#], Paul G. Barghouth[1,2], Salvador Rojas[1,2], Benjamin Ziman[1,2], Eli Isael Maciel[1,2], David Ardell[1,4], Ariel L. Escobar[3,4] and Néstor J. Oviedo[1,4*]

[1]Department of Molecular & Cell Biology, University of California, Merced, USA.
[2]Quantitative and Systems Biology Graduate Program, University of California, Merced, USA.
[3]Department of Bioengineering, University of California, Merced, USA.
[4]Health Sciences Research Institute, University of California, Merced, USA.

#Equal contribution

*To whom correspondence should be addressed: Néstor J. Oviedo,

email: noviedo2@ucmerced.edu
Department of Molecular & Cell Biology, University of California.
5200 North Lake Road, Merced, CA 95343

Abstract:

Exposure to high levels of ionizing γ-radiation leads to irreversible DNA damage and cell death. Here, we establish that exogenous application of electric stimulation enables cellular plasticity to reestablish stem cell activity in tissues damaged by ionizing radiation. We show that sub-threshold direct current stimulation (DCS) rapidly restores pluripotent stem cell populations previously eliminated by lethally γ-irradiated tissues of the planarian flatworm *Schmidtea mediterranea*. Our findings reveal that DCS enhances DNA repair, transcriptional activity, and cell cycle entry in post-mitotic cells. These responses involve rapid increases in cytosolic [Ca^{2+}] through the activation of L-type Ca_v channels and intracellular Ca^{2+} stores leading to the activation of immediate early genes and ectopic expression of stem cell markers in postmitotic cells. Overall, we show the potential of electric current stimulation to reverse damaging effects of high dose γ-radiation in adult tissues. Furthermore, our results provide mechanistic insights describing how electric stimulation effectively translates into molecular responses capable of regulating fundamental cellular functions without the need for genetic or pharmacological intervention.

Keywords: electric stimulation | stem cells | DNA repair | planaria | neoblasts | tissue regeneration | galvanotactic

INTRODUCTION

Since the initial observations made by Luigi Galvani in the late 1700s, scientists have been fascinated by the effects of the exogenous application of electric currents in animal tissues (Adee, 2018; Bresadola, 1998). This long-lasting interest has revealed almost universal roles for electricity during embryonic development, tissue regeneration, and disease (Levin, 2007; Levin, 2014; McCaig et al., 2005). For example, modern FDA approved applications of electric stimulation include deep brain stimulation where indwelling electrodes are implanted in specific regions of the brain to deliver electrical currents and treat diseases such as essential tremors, slow movement, and stiffness in Parkinson disease (Graupe et al., 2018; Miocinovic et al., 2013; Mohammed et al., 2018; Niemann et al., 2017; Velarde et al., 2017). Electric stimulation is also used in treatment-resistant (i.e., refractory) depression, which is the leading cause of disability worldwide (Bewernick et al., 2012; Delaloye and Holtzheimer, 2014; Holtzheimer et al., 2012; Mayberg et al., 2005; Organization, 2018). Recent studies with electric stimulation demonstrate the possibility to restore voluntary control of walking in animals and humans with spinal cord injury (Borgens et al., 1987; Formento et al., 2018; Wagner et al., 2018). Extensive clinical trials, over the past 50 years, demonstrate that direct current stimulation (DCS) improves bone healing by accelerating repair time and reducing pain in nonunion bone fractures (Aleem et al., 2016; Brighton, 1981; Brighton et al., 1981; Griffin and Bayat, 2011; Kuzyk and Schemitsch, 2009; Zhuang et al., 1997).

Additionally, DCS directly applied to the surface of the scalp, (i.e., without implanting electrodes) is known as transcranial DCS (tDCS) and is commonly used in humans (Antal et al., 2017; Chaieb et al., 2014; Chang et al., 2016; Elliott, 2014; Huang et al., 2015b; Kadosh, 2015;

Kadosh et al., 2010; Moreno-Duarte et al., 2014; Nelson et al., 2016; Sarkar and Kadosh, 2016; Tortella et al., 2015). tDCS is widely used to treat many human conditions including motor learning in stroke neurorehabilitation (Boggio et al., 2007), migraines (Antal et al., 2011; Antal et al., 2008), patients with chronic pain (Boggio et al., 2009; Boggio et al., 2008; Borckardt et al., 2012; Mylius et al., 2012), and psychiatric disorders (Tortella et al., 2015). Likewise, cognitive assessments have shown that tDCS can be used to modulate the rate of learning and improve numerical competence in humans (Kadosh, 2015; Kadosh et al., 2010; Snowball et al., 2013). Despite the widespread use of DCS in experimental, clinical, and private settings, the molecular bases of its effects in various cell types remain largely unknown. Together with the rapid proliferation and easy access to devices marketed as direct to customer technology involving electrical stimulation has raised ethical questions, produced confounding results, and created concerns about the risk of potential adverse effects in the body (Coates McCall et al., 2019; Wexler and Reiner, 2019; Wurzman et al., 2016).

The effects of DCS vary depending on the location in the body, the tissue type that is targeted, the intensity of the electric current, and the duration of treatment. Furthermore, the outcome of DCS may differ depending on the context in which it is assayed (i.e., embryonic development, adult stages, disease or homeostasis). It is important to note that currents used in DCS are subthreshold, implying they do not induce action potentials in excitable cells/tissues (Bikson et al., 2004). All cells, including stem cells (SCs), progenitors, and differentiated cells, have built-in mechanisms designed to sense electric changes, which consequently influence their innate cellular transmembrane potential (V_{mem}). Changes in V_{mem} are caused by changes in ion fluxes at the cell plasma membrane (Jaffe, 1981a; Jaffe, 1981b; Levin, 2007; McLaughlin and

Levin, 2018; Nuccitelli and Jaffe, 1974). V_{mem} acts as a potent regulator of cellular migration, proliferation, differentiation, cell cycle, and cell death and is highly sensitive to manipulation by DCS (Levin, 2014; McCaig et al., 2005). Furthermore, DCS, at the organismal level, is capable of altering axial polarity, tissue repair, and organ specification (Borgens et al., 1987; Jaffe, 1981a; Marsh and Beams, 1952; McCaig et al., 2005; McLaughlin and Levin, 2018; Nuccitelli, 2003; Zhao et al., 2006). For example, galvanotactic responses have been observed in migratory cells of humans (Guo et al., 2010), fish (Graham et al., 2013), frogs (Stump and Robinson, 1983), *C. elegans* (Chrisman et al., 2016), and even Paramecium (Ogawa et al., 2006). Similarities in DCS-mediated cellular responses across vertebrate and invertebrate organisms argue for evolutionarily conserved mechanisms.

To further investigate the effects of DCS, we developed an experimental strategy using the planarian flatworm *Schmidtea mediterranea*, known for their high rates of cellular turnover and extraordinary capacity to regenerate tissues that rely in adult SCs called neoblasts (Reddien, 2018; Rink, 2018; Zeng et al., 2018b; Zhu and Pearson, 2016). Neoblasts are known as the only cell with the capacity to divide in asexually reproducing planarians. Thus, neoblast division alone provides the cellular progeny required to renew and repair all planarian tissues (van Wolfswinkel et al., 2014b; Wagner et al., 2011; Zeng et al., 2018b). This constant cellular crosstalk allows planaria to maintain a diverse cellular population through neoblast division, making them powerful models to analyze the effects of DCS on adult SCs and differentiated cells at the cellular, subcellular, and organismal level. Here, we introduced a simplified platform to apply exogenous DCS to the whole body of planarians and analyze the resulting cellular and subcellular responses in real-time. We found that brief exposure to DCS overrides cellular

decisions in tissues exposed to lethal doses of ionizing radiation. Furthermore, our results reveal that DCS is a rapid and robust method with the potential to enhance DNA damage repair, activate transcription of stem cell markers in tissues damaged by ionizing radiation. Moreover, we identified that these DCS-mediated responses are tightly regulated by transcription of immediate early genes and rapid intracellular Ca^{2+} flux. These findings provide insights into the effects of DCS in the adult body, exhibiting their domain over fundamental cellular processes such as transcription, DNA repair, cell cycle, and cellular plasticity without the need for genetic or pharmacological treatments.

RESULTS

Body-wide Application of Steady-State Direct Current (pDCS)

We immobilized planarians by applying our recently developed method (i.e., ThermoPress immobilization), which combines the anesthetic chloretone (0.2%) with a 1% agar-encasing chamber (Davidian et al., 2020). This method of agar immobilization keeps planarians alive while preserving tissue integrity and restricting body movement for hours to days with complete and rapid recovery of sensory functions and locomotion (Fig. 1A). ThermoPress immobilization was used to administer steady-state direct current stimulation to the whole planarian body, which we coined ‘pDCS’ (Davidian et al., 2020).

Electric current was delivered through pulled borosilicate sharp microelectrodes, filled with 3M KCl, placed at the anterior and posterior ventral side of planarian (i.e., pre-pharyngeal and tail, respectively). The microelectrodes resistance was consistently measured at 1-2MΩ. The

control group (sham-treated), consisted of animals exposed to the same procedure, included electrode penetration, with the absence of electric current. To facilitate circuit conduction and minimize electrode byproduct in planarian tissues, microelectrodes were coupled to an electrode bath using 1.0% agar bridges containing 3M KCl solution (Fig. 1B). The amount of current delivered was limited through a 100MΩ resistor, and the most consistent results were obtained when the current traversing the animal was 7μA (Fig. 1C). DCS exceeding 7μA resulted in noticeable tissue damage and eventual animal lysis. All experiments were performed with an electric polarity of a positive pole in the anterior and negative pole in the posterior, unless otherwise stated. Current delivered to the animal was differentially measured and acquired with an analog-to-digital converting board controlled with custom-made LabView-based software (Elliott et al., 2007). Animals were under constant surveillance to ensure that electrode placement and tissue integrity were maintained. Overall, this setup was effective in keeping electrodes correctly positioned and allowed for the analysis of DCS for up to 6 hours.

pDCS activates transcription of stem cell markers in tissues exposed to a lethal dose of ionizing radiation

DCS techniques are known to affect both SCs and differentiated cells in many model organisms (Feng et al., 2017; Huang et al., 2015a; McCaig et al., 2005; Zhao et al., 2006). Planarian neoblasts are generally scattered along the antero-posterior (AP) axis except for regions in front of the eyes or pharynx and uniquely express the gene *smedwi-1* (Reddien et al., 2005; van Wolfswinkel et al., 2014b; Wagner et al., 2011; Zeng et al., 2018b) (*piwi-1* henceforth, Fig. 2A). The *piwi-1* expression is currently used as the standard marker to recognize neoblast presence and distribution (Reddien et al., 2005; Wagner et al., 2011; Zeng et al., 2018b).

166 Exposing planarians to lethal doses of ionizing radiation (60 Gy) irreversibly eliminates
167 neoblasts and corresponding *piwi-1* expression (Fig. 2A); consequently, abolishing their
168 regenerative capabilities. As a result, planarians ultimately perish within three to four weeks
169 following lethal ionizing radiation (Bardeen and Baetjer, 1904; Reddien et al., 2005). However,
170 lethally irradiated planarians can be rescued by transplanting tissue-containing neoblasts
171 (Guedelhoefer and Sanchez Alvarado, 2012a; Guedelhoefer and Sanchez Alvarado, 2012b). This
172 occurs as neoblasts gradually migrate from transplanted tissues to repopulate the entire irradiated
173 host in about a month (Guedelhoefer and Sanchez Alvarado, 2012a). Engrafted tissue becomes
174 more structurally stable after four days post-transplantation (dpt); a stage in which the majority
175 of neoblasts are still within the transplanted tissue. Over the first five dpt, neoblast repopulation
176 is uniform with no bias towards anterior, posterior, medial-lateral tissues (Guedelhoefer and
177 Sanchez Alvarado, 2012a). Thus, this neoblast repopulation paradigm was used as a model to
178 study the effects of pDCS on both adult SCs and differentiated cells in their natural environment.
179
180 Tissue containing neoblasts was transplanted into lethally irradiated hosts and pDCS-
181 treated at four dpt (Fig. 2B). This experimental setup led to essential differences in *piwi-1* gene
182 expression in sham vs. pDCS animals. Specifically, 60 minutes after pDCS, *piwi-1* expression
183 was widely detected outside the transplant toward the posterior region of the animal; whereas, in
184 the sham-treated group, *piwi-1* expression was restricted to tissues adjacent to the transplant, as
185 expected (Fig. 2C). Levels of *piwi-1* expression in the tails of treated planarian increased by
186 more than two-fold as determined by using qPCR (Fig. 2D). Transcriptomic analysis with RNA
187 sequencing from the tail fragment confirmed pDCS treatment for 60 mins was accompanied by
188 an increase in the expression of *piwi-1* (Log2 FC= 1.97, B&H FDR= 0.0006, moderated t= 9.89).

Furthermore, we also detected an increase in the expression of the transcription factor *Smed-soxp-2* (Fig. 2E, Log2 FC= 0.61, B&H FDR= 0.005, moderated t= 4.82), which is a marker of the classic sigma neoblast subpopulation required for stem cell function and planarian regeneration (van Wolfswinkel et al., 2014a; Wagner et al., 2012). Likewise, we observed pDCS slightly reduced the expression of the *piwi* family member *Smed-piwi*-3 after 60 mins of pDCS (Log2 FC= 0.21, B&H FDR= 0.0068, moderated t= 4.24) (Kim et al., 2019; Palakodeti et al., 2008b), while there was moderately upregulation of the late progeny marker *Smed-agat-1* (Fig. 2E, Log2 FC= 0.18, B&H FDR= 0.016, moderated t= 3.74).

We also observed differential expression of other markers (Fig. 2F) associated with the recently expanded neoblast sub-classes (Zeng et al., 2018a). Out of 189 possible Nb markers from the literature 25 markers were differentially expressed with a B&H FDR < 0.05. The transcriptomic analysis tested the contrasts between the 60-minute and sham controls evidencing 1,778 genes differentially expressed and all 25 of these markers are expressed below the 1% level. The transcriptomic analysis for the tissues treated with 60 minutes of pDCS showed key markers for the neoblast sub-classes Nb5, Nb8, and Nb12 were strongly downregulated compared to the control at this timepoint (Fig. 2F). Nb5 and Nb12 contain populations of *Piwi-1*^{high} expressing cells and are hypothesized to include early progenitor cells for intestinal tissue (B&H FDR <0.05). Conversely, markers for the muscle cell progenitors Nb4 and Nb6 (e.g., TDP2, TPI1, and ACTB) were significantly upregulated (Fig. 2F, B&H FDR <0.01). Muscle progenitors are critical for providing positional information and are key drivers of tissue patterning during regeneration (Cote et al., 2019; Scimone et al., 2020; Scimone et al., 2017). Additionally, putative markers for the pharyngeal neoblast progenitors and differentiated

212 populations (Nb7, Nb8, and Nb10) were overall differentially expressed. However, the markers
213 *PTK7* and *PPIC* for the *Piwi-1*^{high} expressing pharyngeal progenitor populations (Nb7 and Nb8)
214 had lower expression compared to the *Piwi-1*^{low} differentiated pharyngeal populations (Nb10)
215 (B&H FDR <0.05). The markers *PDIA6*, *CALU*, and *P4HB* for the Nb10 neoblasts were
216 significantly upregulated after hour-long application of pDCS (B&H FDR <0.05). Only one
217 marker (dd_Smed_v6_1399_0_1) for the putative neural progenitor (Nb11) was significantly
218 upregulated after 60 minutes of pDCS (Fig. 2F, Log2 FC= 0.34, B&H FDR= 40.043, moderated
219 t= 3.71). Importantly, key markers for clonogenic neoblasts (cNeoblasts, Nb2) were significantly
220 upregulated (e.g., *Aats-asp* and *soxP-2*; Fig. 2E, F, Log2 FC> 0.5, B&H FDR <0.01). Our
221 findings show that the hour-long application of pDCS triggers the expression of the pan-neoblast
222 marker *piwi-1* along with markers of neoblast subpopulations with high *piwi-1* expression in host
223 tissues where neoblasts were permanently eliminated by exposure to a lethal dose of ionizing
224 radiation.
225
226 **Lengthening pDCS leads to a directional cell cycle entry in tissues exposed to lethal ionizing**
227 **radiation**
228 pDCS-induced transcription of *piwi-1* in irradiated tissue was also accompanied by an
229 increase in the expression of the neoblast marker *Smed-cyclin B* and other components associated
230 with the regulation of cell division (e.g., cyclin-dependent kinases, mini-chromosome
231 maintenance proteins-MCM-, checkpoint kinase, polo-like kinase, and Rb binding protein), (Fig.
232 2G, H). However, the presence of mitotic cells far away from the transplanted tissue was evident
233 after lengthening pDCS to 6 hours (Fig. 2I, J). Strikingly, the number of mitotic cells outside of
234 the transplant was significantly increased upon pDCS (Fig. 2K). In these animals, mitotic cells

within irradiated tissues were primarily distributed towards the posterior region of the host, being observed as far as the tip of the tail (Fig. 2K). Proportionately, a smaller number of mitotic events occurred in the anterior of pDCS-treated transplanted planarians, implying asymmetrical effects likely due to pDCS polarity (Fig. 2K). In the sham control group, we did not observe asymmetries in dividing cells within the scarce population of mitotic cells outside transplanted tissues (Fig. 2I-K). We also observed variability in the effects of pDCS over mitotic cells. Some animals showed a low/no response (26%) while the large majority displayed moderate effects (67%) by noticeable mitotic signal outside of the transplant (Figure S1A).

To address the possibility of pDCS induced mitotic asymmetry within irradiated tissues, similar magnitude DCS were applied to 4dpt planarian with opposite polarity (i.e., reversed polarity, implying the positive pole located in the tail and the negative pole in pre-pharyngeal tissue in front of the transplant). These experiments led to inconsistent results, thus we decided to continue with the characterization of pDCS based on polarity with positive pole to the anterior and negative implanted in the posterior region of the animal. We also found pDCS displayed similar effects when the tissue graft was placed in the posterior region (Fig. S1B, C). However, tissue transplants in the anterior region were more reliable and convenient to characterize the pDCS effects.

pDCS-induced transcription of stem cell markers originates in lethally irradiated tissues

Exposure to a lethal dose of ionizing radiation permanently eliminates neoblasts in less than 24 hours (Peiris et al., 2016a). Distinctively, pDCS leads to the transcription of neoblast markers and the presence of mitotic cells in the host tissue several days after the exposure to

lethal ionizing radiation. This finding prompted us to investigate the potential source of neoblast-related cells.

First, since the exogenous application of electric fields is widely known to guide movement of cells through electrotaxis (McCaig et al., 2005), we addressed dynamics of cell migration from the transplanted tissue as the potential mediator of pDCS effects. Previous work determined, neoblasts migrate from transplanted tissue to gradually repopulate the lethally irradiated host at a rate of ~3-5µm/hr, which is about 72-120 µm/day (Abnave et al., 2017; Eisenhoffer et al., 2008b; Guedelhoefer and Sanchez Alvarado, 2012a; Guedelhoefer and Sanchez Alvarado, 2012b; Newmark and Sánchez Alvarado, 2000; Reddien et al., 2005; Salo and Baguna, 1985). Because neoblasts are the only dividing cells in planarian, the spatiotemporal path of neoblast-related gene expression and mitotic cells (i.e. mitotic wave) are commonly used to infer migration rates between two points (Abnave et al., 2017; Guedelhoefer and Sanchez Alvarado, 2012a; Guedelhoefer and Sanchez Alvarado, 2012b; Newmark and Sánchez Alvarado, 2000; Salo and Baguna, 1985).

Our results show that following 6hrs of pDCS, mitotic cells are found in the tail of the irradiated host, which is ~5 mm away from the transplanted tissue (Fig. 2I, J). If the transplanted tissue was the source of dividing cells, neoblasts must displace at about 833µm/hr (i.e. ~200 times faster) to arrive at the tip of the tail more than 700 hours earlier than what has previously been reported (Guedelhoefer and Sanchez Alvarado, 2012a; Salo and Baguna, 1985). Furthermore, we found that shorter pDCS leads to a robust *piwi-1* expression throughout the animal (see results below Fig. 5A with 15 mins pDCS). Were this to be the result of cellular

281 migration from the engrafted tissue, neoblasts must migrate at rates exceeding 20,000µm/hr, or
282 2cm/hr; which is not only four orders of magnitude faster than previously established but also
283 unlikely due to physical tissue-derived obstacles in their path.
284
285 Second, recent findings demonstrate cellular migration in planarians depends on the
286 expression of epithelial-mesenchymal transcription factors *Snail-1*, *Snail-2*, *zeb-1,* and the *ß1-*
287 *integrin* gene along with components of matrix metalloproteinase (Abnave et al., 2017; Bonar
288 and Petersen, 2017; Isolani et al., 2013; Seebeck et al., 2017). We compared in sham and pDCS
289 treated animals the expression of markers for cellular migration in two segments, the trunk
290 fragment that included transplanted tissue and the tail region at one hour of treatment (Fig. 3A).
291 The results show that in the trunk the expression increased for both *Snail-1*, *Snail*-2 while there
292 was no change for *zeb-1* and the *ß1-integrin*. In the tail region, we found no changes in the
293 expression except for a slight increase in the *ß1-integrin* gene (Fig. 3B, C). Next, we used BrdU
294 to trace migratory cells, but our attempts were unsuccessful due to inconsistent tissue
295 engraftment likely associated with friability of tissue fragments obtained from donors treated
296 with BrdU.
297
298 Third, we did not observe the anterior to a posterior progressive pattern of neoblast
299 expressing cells nor dividing cells that is characteristic during migration-mediated neoblast
300 repopulation of the irradiated host. For instance, stimulation with pDCS using shorter times (i.e.,
301 15 mins) showed strong expression of *piwi-1* at distant places from the transplanted tissue (see
302 results below Fig. 5A at 15 mins). These findings are in stark contrast to the gradual progression
303 of gene expression of *piwi-1* over the AP axis that takes about 40 days to reach the tip of the tail

304 in the absence of electrical stimuli (Abnave et al., 2017; Guedelhoefer and Sanchez Alvarado,
305 2012b).
306
307 Fourth, we designed a series of experiments involving tissue transplantations between,
308 wild type (WT), *piwi-1(RNAi),* and lethally irradiated animals to measure the expression of
309 neoblast markers in the tail region of the host (Figs. 3D, F, H). We performed selective
310 elimination of *piwi-1* expression in either the host or donor tissue to verify the source of *piwi-1*$^{+}$
311 cells and other progenitor subtypes. It is important to note that *piwi-1(RNAi)* specifically silences
312 *piwi-1* expression without affecting neoblast number or function (Reddien et al., 2005).
313 Transplanting tissue from *piwi-1(RNAi)* animal into a lethally γ-irradiated host resulted in a six-
314 fold increase in *piwi-1* expression in the tail of the host subjected to pDCS compared to sham-
315 treated animals (Fig. 3D, E). The increase in gene expression was also prominent in other
316 neoblast markers, suggesting a generalized neoblast response (Fig. 3E). Since *piwi-1* expression
317 was originally silenced in the transplanted tissue, the increased expression of *piwi-1* away from
318 the transplant; specifically, in the tail suggests, *piwi-1* expression originates in host tissues. To
319 confirm this, tissue containing neoblasts from WT animals was transplanted into *piwi-1(RNAi)*
320 host and subjected to identical treatment (Fig. 3F). The results show that *piwi-1* expression was
321 equivalent to sham-treated as expected, but there was an important increase in the expression of
322 other neoblast markers in the tail of animals with pDCS (Fig. 3G). These findings confirm the
323 specificity of the RNAi strategy and provide evidence in support that lethally irradiated host
324 tissue is the source of expression for neoblast markers upon pDCS.
325

However, it remained unclear whether the presence of neoblast in the graft was needed for the pDCS effects. To address this, neoblasts were eliminated from both the donor and host tissue by lethal γ-irradiation (Fig. 3H). Under these conditions, *piwi-1* expression remained similar to sham control (Fig. 3I), while there was a mixed effect in the expression of markers of neoblast (i.e., most of them were either reduced or did not change except for *sox-P-2,* Fig. 3I). We also noted that application of pDCS in a lethally irradiated animal without transplanted tissue did not trigger expression or neoblast markers or cell division. These results suggest that the presence of neoblasts in transplanted tissue is necessary for pDCS-mediated expression of neoblast markers. Together, our findings indicate that pDCS elicits transcription of SC markers in lethally irradiated tissues, effects that emerge from host tissues but require the presence of grafted neoblasts. Nevertheless, based on the spatio-temporal expression pattern of genes required for migration, the rapid presence of *piwi-1* expressing cells, and cellular division upon short application of electric stimulation, we propose that pDCS-induced effects on neoblast transcription and cell division are not due to electrotactic cellular migration from the transplanted tissue but rather through the activation in the expression of neoblast progenitors and subsequent cell division originating in lethally irradiated host tissue.

pDCS enhances the DNA damage repair response in tissues exposed to a lethal dose of ionizing radiation

Exposure to a high dose of ionizing radiation induces DNA damage and subsequent cell death (Barghouth et al., 2019; Peiris et al., 2016a; Peiris et al., 2016b; Pellettieri et al., 2010). Nonetheless, 60 minutes of pDCS activates gene transcription, a process known to require DNA integrity. Therefore, we assessed DNA integrity and repair mechanisms on dissociated cells

obtained from the lethally irradiated tail region of both the sham-treated and pDCS group. Ionizing radiation increases DNA double-strand breaks (DSBs) that, in planarians, are mainly repaired through homologous recombination (HR) (Barghouth et al., 2019; Peiris et al., 2016b). Immunostainings using markers of DNA damage and repair response were used after 60 mins of treatment in sham and pDCS groups. The results revealed pDCS led to a noticeable increase in phosphorylation of the histone H2AX (γ-H2Ax, Fig. 4A), which is often observed in the early response to DSBs (Bonner et al., 2008; Marti et al., 2006). Likewise, pDCS increased RAD51protein nuclear localization by 20% (Fig. 4B).

Nuclear translocation is essential for the function of RAD51 during DSB repair (Haaf et al., 1999; Peiris et al., 2016b). We further determined, through comet assay, that pDCS-mediated activation of the DDR was accompanied by a noticeable reduction in DSBs caused by γ-irradiation (Fig. 4C). The results were expanded by performing transcriptomic analysis with a focus on genes associated with DNA damage and repair. RNA was extracted from the tail fragments from sham and pDCS animals after 60 mins of treatment and we used BLAST domains as annotations for the transcriptome dd_Smed_v6 (Grohme et al., 2018). When examining orthologs of DNA damage and repair pathways in *H. sapiens* the analysis confirmed genes associated with these pathways were differentially expressed with a majority upregulated (e.g., *ATM*, *RAD17*, *MRE11*, *Rad54B*) (Fig. 4D, E, Supplemental file 1). A gene enrichment analysis was used to identify the strongly activated pathways after 60 minutes of applied pDCS (Supplemental file 2). The biological processes for DNA damage checkpoints and DNA integrity checkpoints (GO:0000077 and GO:0031570) were considered significantly enriched (KS= 0.0424 and significance 33%, respectively). The biological processes for cellular respiration

372 (GO:0045333), generation of precursor metabolites (GO:0006091), and molecular transport
373 (GO:0008272, GO:0015698, GO:0015698, GO:0072348) were the most highly enriched
374 biological processes. Cellular component genes involved with the nucleus were considered the
375 most enriched cellular components at this time point (Supplemental file 2). This is supported by
376 the enriched molecular functions for nucleotide-binding (GO:0000166), RNA binding
377 (GO:0003723), translation factor activity, RNA binding (GO:0008135), and additional functions
378 involved in nucleic acid activity (Supplemental file 2). The most enriched functions upregulated
379 by pDCS compared to the sham control were catalytic activity (GO:0003824) which showed that
380 21% of genes annotated with this term were significantly differentially expressed (Supplemental
381 file 2). These data suggest nucleic acid activity is highly enriched upon an hour-long application
382 of pDCS.
383
384 In addition to the upregulated DNA repair and DNA damage transcripts, there was a
385 strong upregulation of transcripts associated with replication (Fig. S2, Supplemental file 1).
386 Approximately 60% of significantly differentially expressed genes related to replication were
387 upregulated and further supports the notion that nucleic acid activity is enriched upon application
388 of hour-long pDCS treatment. pDCS effects were also accompanied by improvements in cell
389 viability as determined by flow cytometry with annexin V and immunostaining using Caspase-3
390 antibody (Peiris et al., 2016a; Thiruvalluvan et al., 2018). We did observe reduced levels of pre-
391 apoptotic cells compared to the sham-treated group (Fig. 4F). Consistently, we also noticed a
392 reduction in pro-caspase-3^{+} cells that are commonly associated with pre-apoptotic cells (Fig.
393 4G). These results were accompanied by differential expression of genes known to regulate
394 apoptosis (Fig. 4H, Supplemental file 1). In summary, these findings demonstrate that 60

minutes of pDCS is capable of activating DNA repair, DNA damage, and replication mechanisms leading to reduced overall DNA damage in lethally γ-irradiated tissues.

pDCS activates transcription of immediate early genes in lethally irradiated tissues

Previous work demonstrates the capacity for electric stimulation to produce rapid cellular responses, beginning at the transcriptional level (Dragunow and Robertson, 1987; Saha et al., 2011). To determine if pDCS treatment is capable of influencing transcription of neoblast markers on a more rapid time scale, tissue from WT animals was grafted into lethally irradiated hosts and exposed to different lengths of pDCS (i.e., 15, 30, 45 min; Fig. 5A). Strikingly, expression of *piwi-1* and other neoblast markers were not only detected but found maximally enriched during the first 15 min of pDCS (Fig. 5A-C). The expression of these neoblast-specific genes gradually reduced over time (Fig. 5A-C). Transcriptomic analysis using tail fragments from the 15 mins timepoint showed a strong upregulation in the expression of *Smed-SoxP-2, Smed-Agat-1, piwi-1-3* that are markers of the sigma and pan-neoblast populations according to the classic classification (Fig. 5D, B&H FDR <0.05, Supplemental file 3) (Eisenhoffer et al., 2008a; Kim et al., 2019; Palakodeti et al., 2008a; van Wolfswinkel et al., 2014a). Moreover, we also detected significant differential expression of 35 out of 189 markers (Fig. 5E) associated with various neoblast subclasses (Supplemental file 3) (Zeng et al., 2018a). In general, there was a strong upregulation in the expression of markers associated with cNeoblast (Nb2) and progenitors of the pharynx, (Nb7), epidermal (Nb1), and muscle (Nb4, Nb6) after 15 mins of pDCS (Fig. 5E, B&H FDR= 0.05, Supplemental file 3**).**

This rapid upregulated transcription pattern was also observed in markers of DNA damage response, DNA repair, and DNA replication (Fig. S3A-C). A gene Set Enrichment Analysis (GSEA) with the topGO Komogorov-Smirnoff test of these data shows the most enriched biological processes occurring after 15 minutes of pDCS are related to metabolic and transport processes (Supplemental file 2). This is also consistent with 40% enrichment of genes related to the mitochondrial outer membrane (GO:0005741). The most enriched molecular function at this early timepoint were genes related to the catalytic activity (GO:0003824) where 21.7% (413) genes were found significantly enriched. RNA binding activity (GO:0003723) genes showed enrichment with 19.6% of genes being significant (Supplemental file 2). Overall, the enrichment analysis suggests DNA damage, repair, and cell cycle processes are activated early upon application of pDCS. Plotting statistically significant genes orthologous to all genes involved in DNA damage, DNA repair, and replication pathways was consistent with the identification of upregulation in critical DNA repair genes. For example, Rad54 and Rad51 are upregulated with a LogFC increase greater than 1.2 (Fig. S4B, B&H FDR= 0.05). Checkpoint Kinase 1 (CHK1) is a critical mediator of DNA damage response and cell cycle activation and upregulated by 1.7-fold with early application of pDCS (B&H FDR= 0.01, moderated t= 5.98). DNA polymerases, helicases, and topoisomerases are upregulated two-fold. Cyclin-dependent kinase 1 (CDK1) exhibits the strongest increase of expression by nearly four-fold and further demonstrates the strong activation of cell cycle pathways (B&H FDR= 0.0046, moderated t= 4.72). In comparison, the expression of CHK1 and CDK1 at the 60 mins timepoint is slightly dampened which supports the high enrichment of cell cycle regulators in the GSEA after 15 minutes pDCS (Supplemental file 2). The results indicate pDCS elicits a rapid transcriptional

response geared toward markers of neoblast, DNA damage, and repair within the hosts irradiated tissues.

These remarkably rapid changes in gene expression after pDCS are temporally consistent with activation of immediate-early gene (IEG) transcription, generally defined as genes expressed in the absence of *de novo* protein synthesis (Bahrami and Drablos, 2016; Greer and Greenberg, 2008; Herschman, 1991; Morgan and Curran, 1991; Saha and Dudek, 2013). Furthermore, the mRNA of IEGs are detectable within minutes of exposure to a wide range of stimuli such as stress, mitogens, immune response, neuronal signals, and electric stimulation (Bahrami and Drablos, 2016; Cohen and Greenberg, 2008; Greer and Greenberg, 2008; Saha and Dudek, 2013). pDCS time-course qPCR results show a rapid and transient expression of a well-characterized member of the IEG family, *early growth response gene-1* (*egr-1,* Fig. 5C), which is a well-characterized member of the IEG family (Bahrami and Drablos, 2016; Greer and Greenberg, 2008) and an established neoblast marker required for regeneration and stem cell function in planarians (Lei et al., 2016; Sandmann et al., 2011; Tu et al., 2015a; Wagner et al., 2012; Zeng et al., 2018a).

IEGs are classified based on their induction profile and separated into rapid, delayed, or slow expression response groups following a stimulus (Bahrami and Drablos, 2016; Saha and Dudek, 2013). Thus, we compiled a list of 138 known IEGs previously reported in other model organisms (Figure S4) (Cullingford et al., 2008; Tullai et al., 2007; Uhlitz et al., 2017) and matched the respective expression of their putative planarian orthologs following pDCS. Genes that were considered significantly differentially expressed at the 15mins timepoint were listed

following *p*-value and FDR cut-offs of <0.05; this yielded a total of 1778 up-regulated genes. Out of 1778 genes we found 25 planarian orthologs to published IEGs in the 15min pDCS treated planarian (Fig. 5F, S4). This analysis confirmed the upregulated expression of *egr-1* and revealed that the increased expression of IEGs persists through the hour-long application of pDCS (Log2FC= 1.32, B&H FDR= 0.0013, moderated t= 7.42). Additionally, other members of the immediate early genes were considerably upregulated after 15 mins pDCS treatment including the RAS oncogene and the dual-specificity phosphatase 10 (DUSP10) that is known to affect components of the mitogen-activated protein kinases (MAPKs), JNK and ERK (Fig. 5F). Within the 25-planarian putative IEGs we found representation for all three subclasses (IEG, DEG, and ILG) and the number of upregulated and downregulated members of those groups were split. It is not entirely clear how pDCS transcriptional regulation of IEGs is translated into cellular actions, but our observations suggest that short treatment with pDCS stimulates the rapid induction of IEGs within lethally irradiated tissues.

pDCS induces ectopic expression of neoblast markers mediated by Ca^{2+} signaling

Since exposure to a lethal dose of irradiation irreversibly eliminates neoblasts, we assessed the identity of host-cells expressing neoblast markers following 15 minutes of pDCS. To recognize the spatiotemporal distribution of cells at different stages of differentiation, we performed expression analysis using double fluorescent *in situ* hybridization (FISH) in tissue sections (Fig. 6A). Specific genes were chosen to reflect two distinct stages of cellular differentiation, *piwi-1* and *agat-1*, which label early progenitors and late post-mitotic progeny, respectively (Eisenhoffer et al., 2008b). Our results show that 15 min pDCS induces a 56-fold increase in *piwi-1*$^{+}$ cells and this upregulation coincides with a simultaneous 21-fold increase in

485 *agat-1*$^{+}$ cells (Fig. 6B, C). Intriguingly, 70.1% of *agat-1*$^{+}$cells co-express *piwi-1* while 24.5% of
486 *piwi-1*$^{+}$ cells co-express *agat-1* (Fig. 6B). Moreover, sham control planarian exhibited minimal
487 *piwi-1*$^{+}$/*agat-1*$^{+}$ cells, as expected in 4-day post-irradiated tissue (Fig. 6A, C). Previous research
488 reported minimal, if any, the overlap between *piwi-1* and *agat-1* occurs in WT planarian (<
489 2.0%) (Eisenhoffer et al., 2008b). The ectopic expression of the neoblast marker in post-mitotic
490 cells suggests that the brief application of pDCS disrupts patterns of gene expression across
491 cellular lineages.
492
493 Calcium signaling is among the most prominent mediator of excitation-transcription
494 coupling and IEG activation (Greenberg et al., 1986; Greer and Greenberg, 2008; Saha and
495 Dudek, 2013; Saha et al., 2011; Yan et al., 2014). For example, voltage-dependent calcium
496 channels at the plasma membrane can be electrically stimulated to allow the rapid influx of Ca^{2+}
497 to the cytoplasm (Yan et al., 2014). Similarly, calcium signaling mechanisms have been
498 suggested as mediators of acute signaling events in various experimental models, including
499 planarian (Bahrami and Drablos, 2016; Chan et al., 2017; Cohen and Greenberg, 2008;
500 Greenberg et al., 1986; Greer and Greenberg, 2008; Herschman, 1991; Kandel, 2012; Ma and
501 Yan, 2014; Marchant, 2019; Morgan and Curran, 1991; Saha and Dudek, 2013; Saha et al., 2011;
502 West and Greenberg, 2011; Yan et al., 2014). In concert with these reported findings, inhibiting
503 calcium flux through L-type voltage-gated calcium (Ca_v) channels using a dihydropyridine
504 (DHP), nicardipine, dramatically suppressed the effects of rapid (15 min) pDCS-mediated
505 expression of neoblast markers (Fig. 6D, G, J). The effects of nicardipine inhibition persist even
506 if pDCS was extended to 60 minutes (Fig. S5 A-C). These results were confirmed with
507 nifedipine, another DHP that blocks L-type Ca_v channels via a different high-affinity binding site

(Fig. S5 D-G). Likewise, buffering of intracellular Ca^{2+} with EGTA-AM [ethylene glycol-bis(ß-aminoethyl ether)-N,N,N',N'-tetraacetoxymethyl ester] also disrupts pDCS-mediated *piwi-1* and *agat-1* expression (Fig. 6H, E, G, K). These results suggest that Ca^{2+} released from intracellular Ca^{2+} stores (i.e., endoplasmic reticulum) mediate pDCS effects.

DISCUSSION

Our findings underscore the overriding capacity of bioelectric signaling to rapidly affect essential cellular processes such as transcription, cell cycle, and DNA repair. This robust and effective strategy is capable of altering cellular behavior *in situ*, without the need for genetic or pharmacological intervention. The results in planarians are consistent with the overriding effects obtained with DCS in mice models of the Rett syndrome (RTT). The RTT is caused by inactivation of the X-linked gene methyl-CpG-binding protein 2 (*MECP2*) (Amir et al., 1999) and is a complex degenerative dysfunction involving many genes and neuronal groups, in which pharmacotherapy is unlikely to succeed (Baker et al., 2013; Chahrour et al., 2008; Johnson et al., 2017; Sugino et al., 2014). However, application of DCS with electrodes implanted in the brain of RTT mouse model, activate neurogenesis and restore neural circuits and spatial memory, and the behavior of the experimental group is indistinguishable from sham-treated mice (Hao et al., 2015; Lu et al., 2016; Pohodich et al., 2018). Jointly, the results in both vertebrate and invertebrates suggest the overriding effects of DCS (pulsing or steady-state) consistently overcome conditions involving dysfunctional DNA.

We introduce planarians as a simplified platform to carry out comprehensive analysis aimed at dissecting the molecular basis of electric stimulation at the organismal, cellular, and

subcellular levels. We observe extensive commonalities between DCS effects in planarians and mammals. For example, the time and strength of the currents used in our DCS are similar to the ones used in humans (e.g. tDCS, muscle, bone repair) (Gerovasili et al., 2009; Kadosh et al., 2010; Moreno-Duarte et al., 2014). Ca^{2+} signaling consistently recurs as a mediator of DCS effects in planarians and mammals. Likewise, the overall changes upon pDCS are transient, thus providing self-contained regulatory mechanisms that can be calibrated to gain desired cellular responses under different circumstances. Uniquely, our findings demonstrate a cost and time-effective alternative to study rapid activation of transcription in tissues exposed to high doses of ionizing radiation. DNA damage is central to cancer, aging, and radiotherapy, but there are limited options to effectively enhance genomic repair. We present evidence demonstrating short exposure to pDCS activates transcription of genes involved in the DDR, which together lead to the reestablishment of DNA integrity in tissues exposed to a high dose of ionizing radiation. Future experiments will be designed to address both the fidelity of pDCS-induced DNA repair and the molecular mechanism mediating this process. One possible candidate may involve small non-coding RNAs (sncRNAs), which recent evidence shows may facilitate the recruitment of repair components in both HR and NHEJ to sites of DSBs (Gao et al., 2014; Qi et al., 2016; Wei et al., 2012).

pDCS triggers the ectopic transcription of stem cell and differentiated tissue markers followed by mitotic activity in tissues damaged by ionizing radiation. The molecular mechanism of this intriguing finding is still unclear, but it is possible that pDCS may affect cell fate regulators associated with the lineage progression of post-mitotic progenitors to increase cellular plasticity. Indeed, our finding showing overlapping expression of *agat-1* and *piwi-1* in post-

554 mitotic cells is consistent with recent findings demonstrating enhanced cellular plasticity by
555 disturbing hippo and *egr-5* signaling pathways (de Sousa et al., 2018; Tu et al., 2015b).
556 However, to our knowledge, there is no precedent in which a short electric stimulus can robustly
557 coordinate genetic and cellular events toward stem cell reconstitution in tissues damaged by
558 ionizing radiation. Future studies will be needed to understand the epistatic relationship between
559 cell fate regulators and the identity of the cells expressing neoblast markers ectopically along
560 with the long-term stability of the *piwi-1*$^{+}$ cells.
561
562 One possible explanation driving the pDCS-mediated expression of stem cell markers is
563 that distinctive post-mitotic progenitors can sense the electric stimulus and respond. Consistent
564 with this idea, we propose post-mitotic lineages expressing L-type Ca_v channels [i.e., neural,
565 epidermal, parenchymal, protonephridia, and cathepsin^{+} cells (Fincher et al., 2018; Plass et al.,
566 2018)] are likely the targets of pDCS-enhanced plasticity (Fig. S6). Future experiments will
567 address the individual contribution of post-mitotic lineages expressing L-type Ca_v channels after
568 pDCS. Another possible scenario may involve the presence of radio-resistant neoblasts or
569 neoblasts with low cycling activity that are sensitive to the electric stimulus. Recent evidence
570 supports the possibility of slow-cycling neoblasts with distinctive regenerative properties
571 (Molinaro et al., 2021). The complete picture of the neoblast heterogeneity and their regulation is
572 an evolving subject that is far from being understood (Fincher et al., 2018; Molinaro and
573 Pearson, 2016; Plass et al., 2018; Reddien, 2018; Rink, 2018; van Wolfswinkel et al., 2014b;
574 Wagner et al., 2011; Zeng et al., 2018b).
575

We propose a model whereby pDCS may lead to enhanced DNA repair followed by transcription. Our results implicate pDCS effects are mediated by increases in intracellular [Ca^{2+}] concentration via L-type Ca_v channel and/or release from intracellular Ca^{2+} stores (Fig. 7A). The initial effects of pDCS stimulate transcription of IEGs that are tightly regulated by increases in intracellular [Ca^{2+}] concentration via L-type Ca_v channel and/or release from intracellular Ca^{2+} stores (Fig. 7B). The increase in cytosolic [Ca^{+2}] may serve to boost DNA repair improving DNA integrity followed by the transcription of IEGs (Fig. 7B). The outcome of these Ca^{2+} mediated events significantly reduce overall levels of DNA damage leading to transcription of stem cell-related genes and cell cycle re-entry in tissues damaged by ionizing radiation. Further experiments are needed to determine the order in which these events take place and to further define the identity of the cells expressing neoblast markers. It is unclear whether radio-resistant cells, slow-cycling neoblasts, or post-mitotic cells with enhanced plasticity are associated with pDCS-induced effects (Fig. 7C).

Material and Methods

Planarian culture and maintenance

For transplantation experiments, planarians were acclimatized to a final culturing temperature of 13°C. Acclimatization was gradual, beginning with an initial transfer to 16°C for approximately two weeks and then stepped to 13°C permanently until planarian were used for transplantation. Before each change in temperature, planarian cultures, destined for transfer, were fed before temperature changes. Animals transferred to 13°C incubators were cleaned once per day for the first four days of temperature acclimatization. All planarian maintenance was performed as previously described (Oviedo et al., 2008b). After the first four days, planarian maintenance was resumed as previously described (Oviedo et al., 2008b). Planarians were not used for tissue transplantation until they had been cultured for at least two weeks at 13°C. Reduced culturing temperatures were used to decrease the mobility of recovering planarian following tissue transplantation.

Tissue Transplantations

Planarians were transplanted as previously described (Guedelhoefer and Sanchez Alvarado, 2012a; Guedelhoefer and Sanchez Alvarado, 2012b) with minor changes to tools used for transplanting tissue. We developed a transplantation tool to facilitate consistency in the size of the graft and reduce tissue damage. Briefly, the transplantation tool was made from a 19-18$\frac{1}{2}$ gauge syringe that was bored out to an inner diameter of 750µm using a Dremel drill bit. The outer diameter was polished using 500-1000 grit wet sandpaper until the edges were paper thin and smooth to reduce drag during tissue insertion.

615 Transplantation schedules varied with respect to experimental condition (i.e. WT,
616 irradiated, or RNAi tissues). Specifically, in experiments using irradiated planarian host or donor
617 tissue, all irradiation was performed 24hours before tissue transplantation. For transplantation
618 experiments using piwi-1 RNAi tissues, transplantation was performed 48hrs post-final injection
619 (5^{th} injection) and subsequent pDCS experiments occurred 4 days post-transplantation.
620 Additionally, in transplantation experiments using *piwi-1* RNAi planarian, all *piwi-1* RNAi
621 donor tissue was derived from *piwi-1* RNAi hosts (i.e. *piwi-1* donor inserts were taken from the
622 anterior region of intact *piwi-1* RNAi who were then used as hosts for wild-type donor tissues).
623
624 **Planarian Immobilization**
625 Transplanted or intact planarians were placed in chilled 0.2% w/v chloretone solution for
626 3-5 minutes (Guedelhoefer and Sanchez Alvarado, 2012a; Guedelhoefer and Sanchez Alvarado,
627 2012b) in preparation for agar immobilization. After soaking, the planarians were rinsed in
628 chilled planarian water. Motionless planarians were individually placed on large 75mm x 50mm
629 glass slides roughly 1.0 cm apart, atop the ice. All remaining planarian water was removed, and
630 planarian were subsequently covered in 1.0% low melting point agarose (1.0% w/v LMP agar,
631 planarian water) (ThermoFisher 16520050), nearing room temperature, until the planarians were
632 entirely submerged. Planarians were gently positioned to level during the gelation process to
633 achieve maximum body axis symmetry. Once the agar is completely solidified, excess agar was
634 trimmed and encapsulated planarians were placed into the center of chilled 35mm Petri dishes
635 (Corning CLS430588), prefilled halfway with solidified 1.0% agarose (1.0% agar w/v, planarian
636 water) (Sigma A9539). The remaining petri dish volume was filled with 1.0% agarose until the

637 agarose level is flush with the top of the encapsulated planarian. All agar encapsulation processes
638 were performed on ice.
639
640 **Administration of current and electric field generation for pDCS experiments**
641 Planarians were immobilized in agarose and subjected to applied currents via current
642 clamped microelectrodes. To deliver the current, a power supply was fashioned using thirty 9V
643 batteries in series sectioned in 45V increments; the power supply is fashioned with a 100K rotary
644 potentiometer to adjust output to the desired voltage.
645 To deliver the current to the planarians, borosilicate sharp microelectrodes were pulled
646 using the P-97 Flaming/Brown pipette puller (Sutter Instruments P-97). Microelectrodes were
647 filled with 3M KCl and placed vertically in a 3M KCl bath with the pulled tip in solution. To
648 deliver current to the planarians, microelectrodes were bridged with 6-8" long 1/32" I.D. PVC
649 tubing filled with 3M KCl 1.0% agar connected to 3M KCl baths joined to the power supply via
650 Pt electrodes. The current was clamped using an RNX 3/8 1GO 100MΩ resistor (Mouser RNX-
651 3/8-100M) in series with the planarian.
652 For all pDCS experiments, the power supply output was 70V (7μA delivered to
653 planarian) and immobilized planarian were impaled through their ventral epithelial layer, in the
654 pre-pharyngeal region, proximal to the brain, and the tail tip, with each glass microelectrode. The
655 duration of current administration ranged from minutes to hours depending on the needs of the
656 experiment. The polarity of the electric field in this paper was positive pole in the anterior and
657 negative to the posterior region of the animal.
658
659 **Library Preparation and RNA Sequencing**

660 Planarians treated with pDCS and sham transplanted planarian tails were isolated, and RNA was
661 extracted for each sample. pDCS and sham planarian for these experiments were planarians with
662 wild-type donor tissue transplanted into 24 hours irradiated host tissue. Triplicated analysis was
663 performed for each data point that consisted of pooled samples from four planarian tails per
664 replicate. RNA libraries were prepared and sequenced on the Illumina HiSeq 4000 platform at
665 the DNA Technologies Core at the UC Davis Genome Center. Samples were indexed and pooled
666 for multiplexing. All samples were analyzed using a Bioanalyzer for quality control before
667 sequencing.
668
669 **RNA Isolation**
670 RNA from tissues was extracted as previously described (Oviedo et al., 2008c). Tail fragments
671 from sham and pDCS animals were placed in Trizol immediately after amputation and RNA was
672 extracted for each sample. Triplicated analysis was performed for each data point that consisted
673 of pooled samples from four planarian tails per replicate.
674
675 **Library Preparation and RNA Sequencing**
676 The cDNA sequencing libraries were prepared using an automated system at the UC Davis
677 Technologies Core. All samples were accompanied with quality control (QC) documentation and
678 profiled with Bioanalyzer for QC before sequencing. Poly-A enrichment was used to remove
679 ribosomal RNA contamination and maximize mRNA detected. Samples were indexed and
680 pooled for multiplexing. Using the Illumina HiSeq 4000 platform, paired-end reads were
681 sequenced to a length of 200 bp by the DNA Technologies Core at the UC Davis Genome
682 Center. This generated high-quality RNA-seq data for thorough downstream bioinformatic

683 analysis to detect delicate changes in phenotype. Paired-end sequencing was also used to resolve
684 ambiguous differences with high repeat regions.
685
686 **Read Mapping and Gene Expression Analysis**
687 Trimmed fastq files were assessed for quality control and mapped to the recently
688 published complete *Schmidtea mediterranea* genome dd_Smes_g4_1 from the PlanMine
689 database (Grohme et al., 2018). The Bioconductor package Rsubread version 2.4.2 (Liao et al.,
690 2013) was used to map reads to the reference genome using a robust and efficient seed-and-vote
691 algorithm followed by the featureCounts algorithm to assign counts. The raw counts' data were
692 normalized and filtered for genes with log2 counts-per-million (CPM) greater than 0.5
693 (Supplemental file 4). The sample variation was assessed for quality. A customized pipeline
694 using the limma package and voom transformation for precision weights was developed (Law et
695 al., 2014; Phipson et al., 2016; Ritchie et al., 2015). Limma version 3.46.0 and edgeR version
696 3.32.1 were used for the statistical analysis. Test statistics were produced using empirical Bayes
697 moderation, and subsequent heatmaps were made using the ComplexHeatmap Bioconductor
698 package. We separately tested the contrasts of gene expression in the 15-minute and 60-minute
699 conditions against that in the sham control using a Benjamini-Hochberg False Discovery Rate of
700 5%. All bioinformatic analyses were coded with R version 4.0.3 on macOS Big Sur 10.16 using
701 the x86_64-apple-darwin17.0 platform.
702
703 **Gene Set Enrichment Analysis**
704 Gene Set Enrichment Analysis was performed using the Bioconductor topGO package version
705 2.42.0. (Alexa and Rahnenfuhrer, 2020; Alexa et al., 2006). Gene Ontology annotations for the

dd_Smed_v6 transcriptome were mined from the Planmine database and used to map pathway enrichment (Alexa and Rahnenfuhrer, 2020; Grohme et al., 2018). Gene rankings calculated by the Limma-voom pipeline were used for determining the significance and enrichment (Alexa et al., 2006; Law et al., 2014; Liu et al., 2015; Phipson et al., 2016; Ritchie et al., 2015; Smyth and Speed, 2003). Enrichment was computed by ranking gene scores using the conservative Kolmogorov-Smirnov (K-S) test. Pathways were considered enriched with a K-S p-value <0.05. A complete RMarkdown-based notebook of code to reproduce the transcriptomic and GSE Analysis is available in Supplementary Online Materials.

Ca^{2+} inhibition via Nicardipine, Nifedipine, and EGTA-AM

Nicardipine and nifedipine inhibition was performed on transplanted planarian 3 days post-transplantation such that the 24hr incubation period concluded at 4 days post-transplantation. Each dihydropyridine was dissolved in 100% DMSO at a concentration of 10mM and then diluted in 50mL of planarian water to a final working concentration of 5µM, as described previously (Nogi et al., 2009). EGTA-AM administration as achieved via posterior injections 1hr prior to pDCS delivery. Firstly, planarian volume was estimated using $\frac{1}{2} \cdot (\frac{4}{3}\pi abc)$ where a, b, and c represent planarian length, width, and height. With estimated planarian volume, EGTA-AM was diluted in Milli-Q water and injected (37nL per injection pulse) such that the final EGTA concentration was 100µM.

Tissue preparation for cryosections

Planarian are fixed using NAC-formaldehyde based fixation as described previously (King and Newmark, 2013). Fixed animals were prepared for cryosectioning as previously

729 described (Reddien et al., 2005). Briefly, planarians were immersed in increasing concentrations
730 of sucrose diluted in 1XPBS. 1XPBS was replaced with 15% sucrose solution for 1 hour and
731 then 30% sucrose solution overnight at 4°C. Planarians were then placed in tissue embedding
732 molds; 30% sucrose was removed and replaced with optimal cutting temperature (OCT)
733 medium. Planarians were then situated to the desired position/orientation within the OCT and
734 molds were quickly placed in cooling bins containing dry ice immersed in 2-methyl-1-butanol.
735 Once frozen, samples were stored at -80˚C until needed for sectioning. The tissue was sectioned
736 in a Leica Cryostat CM1860. Sectioned tissue was either used immediately for FISH/IHC or
737 stored long-term at -80˚C until needed.
738
739 **Fluorescent *in situ* hybridization (FISH) on sectioned tissue**
740 Cryo-section containing slides were removed from storage at -80˚C and given 30min to
741 reach room temperature. Clear scotch tape was placed over the frosted label to ensure label
742 longevity and assist in coverslip placement during hybridization. Custom-made multi-slide
743 chambers were developed and used throughout the procedure. Multi-slide chambers held 12
744 slides and only required 16ml of the solution to reach maximal coverage. Standard Coplin Jars
745 may be used but require more solution volume per slide contained. After slides reached room
746 temperature, slides were placed in the chamber and rehydrated in 1XPBS for 15min (x2).
747 Following rehydration, FISH was performed as described in (King and Newmark, 2013) with
748 specific changes, as follows: proteinase K incubation was performed for 10min at room
749 temperature at 1µg/mL PK concentration. 1:1 prehybridization/PBStx was omitted. For pre-
750 hybridization and hybridization solution incubation, slides were removed from the chamber and
751 placed in repurposed slide holding containers (converted to hybridization chambers using water-

752 saturated tissue paper placed in each column (x2)) 150µL of the solution was administered to
753 slides, and then glass coverslips were placed atop slides to seal in solution, decreasing
754 evaporation. At the end of the FISH procedure, DAPI (1:1000) was added to slides within the
755 multi-slide chamber for 30min and washed (x2) with 1XPBS. Slides were mounted using the
756 Gelvatol solution.
757
758 **Fixation of large planarian for in-situ hybridization**
759 All large planarian (8-12mm) used for whole-mount *in-situ* hybridization (WISH) were
760 fixed using a modified NAC fixation protocol previously described (Guedelhoefer and Sanchez
761 Alvarado, 2012a). Changes for fixation were introduced as follows: planarian first underwent
762 $MgCl_2$ tissue relaxation as described in (Forsthoefel et al., 2014). Briefly, planarians were placed
763 in 0.66M $MgCl_2$ for 45-60s until planarian fully relaxed. The $MgCl_2$ solution was replaced with
764 10% N-Acetyl cysteine for 10min at room temperature. Lastly, bleaching was performed with a
765 modified bleaching solution (0.5% formamide, 0.36% H_2O_2, 0.05% Triton X-100, 1X PBS) and
766 placed under light, overnight.
767
768 **Whole-mount in-situ hybridization (WISH)**
769 WISH was performed following a previous protocol (Guedelhoefer and Sanchez
770 Alvarado, 2012a). Minor modifications were made during proteinase K treatment, doubling the
771 concentration to 2mg/mL, treating samples for 10min at room temperature.
772
773 **Whole-mount immunohistochemistry (IHC) and analysis**

774 Planarians were fixed for IHC following standard formaldehyde-based fixation with an
775 added formamide based step as described previously (Guedelhoefer and Sanchez Alvarado,
776 2012a). Cells counted positive for Histone H3 phosphate signal (H3P) were normalized against
777 the planarians surface area (mm^2). When counting H3P in transplanted planarian, the anterior-
778 posterior axis margin was shifted to the center of the transplant. Total $H3P^+$ cells were then
779 counted in relation to the population of $H3P^+$ cells within the transplant. Briefly, total $H3P^+$ cells
780 were counted in host tissue, specifically excluding cells within the transplanted tissue, to $H3P^+$
781 cells restricted in the anterior or posterior regions within sham and pDCS planarian
782 independently (% cells outside transplant). Cell counting was performed using NIH ImageJ cell
783 counter plugin, and all data analysis was performed in Prism.
784
785 **Fixation and IHC on dissociated cells**
786 Planarian tail portions were separated and homogenized following pDCS. Homogenate
787 was suspended in calcium and magnesium-free media (CMF) and placed on ice. Cell density was
788 quantified using hemocytometers and cells were plated at 1million/cm^2 onto glass coverslips.
789 Cells were given 1hour to adhere to the surface and were then fixed with Carnoy's solution for
790 2hours on ice. IHC was performed using the human anti-RAD51 antibody and γH2AX antibody
791 as previously shown (Peiris et al., 2016b; Thiruvalluvan et al., 2018).
792
793 **RNAi experiments**
794 RNAi was carried out via dsRNA micro-injection (Oviedo et al., 2008a). *piwi-1* and *nelfB*
795 RNAi consisted of 3 consecutive injections followed by one weekly injection until animals were
796 utilized for experimentation (14days post first injection). Injections were administered to the

797 prepharyngeal regions and, due to the size of the planarian (8-12mm), each planarian was given
798 6-8 pulses of dsRNA 37nL each. *piwi-1* gene was selected and identified using the SmedGD
799 database (Robb et al., 2015). dsRNA was synthesized in vitro as previously described (Oviedo et
800 al., 2008a).
801
802 **Quantitative real-time PCR**
803 Quantitative real-time PCR was performed as described (Peiris et al., 2016b). The
804 ubiquitously expressed gene H.55.12e was used as a reference control. Experiments were
805 conducted in triplicates for each condition. Each qPCR experiment was conducted
806 independently at least two times. All qPCR experiments used RNA extractions from tails of
807 pDCS and sham transplanted planarian unless otherwise specified (i.e. qPCR for migratory
808 related genes used tissue sections across the planarian as described in the text). Extracted RNA
809 was then converted to cDNA using the Verso cDNA synthesis kit (ThermoFisher AB1453A).
810 Gene expression is expressed in fold change in comparison to the given control condition.
811
812 **FACS Analysis and Comet assay**
813 FACS and comet analyses were performed as previously described (Peiris et al., 2016a;
814 Peiris et al., 2016b).
815
816 **Imaging and data processing**
817 All images were captured using a Nikon AZ-100 multi zoom microscope equipped with
818 NIS Elements AR 3.2 software. The brightness and contrast of digital images captured in NIS
819 Elements software were further adjusted in Photoshop (Adobe). Area calculations and cellular

820 foci quantification were carried out using NIH ImageJ software. Mitotic counts were normalized
821 against the planarians' surface area using ImageJ.
822
823 **Statistical Analysis**
824 Data are expressed as the mean ± standard error of the mean (SEM) or fold change ± SEM.
825 Statistical analysis was performed in Prism 2015 software, Graphpad Inc.
826
827 **Data Availability**
828 All raw and processed data files associated with this study have been deposited to the NCBI
829 Sequence Read Archive (SRA) submission number SUB8831617. The bioinformatic and RNA-
830 seq analyses pipeline with metadata files are found on the Github repository at:
831 https://github.com/mlegro/RNA-seq-of-pDCS.

832 **Acknowledgments:** We thank Edelweiss Pfister for lab managing and planarian maintenance,
833 and members of the Oviedo lab for insightful discussions and comments on the manuscript. We
834 are grateful to Ivy Pham for assistance with the planarian recovery experiments upon
835 immobilization and Dr. Richard Nuccitelli for advice and critical reading of the manuscript. The
836 sequencing was carried out by the DNA Technologies, and Expression Analysis Cores at the UC
837 Davis Genome Center, supported by NIH shared instrumentation grant 1S10OD010786-01. We
838 thank Monica Britton and Blythe Durbin-Johnson of the UC Davis Bioinformatics Core facility
839 for advice with transcriptomic analysis. This work was supported by the National Science
840 Foundation (NSF) graduate fellowship award 1744620 to EIM, and the University of California
841 Cancer Research Coordinating Committee (Award# CRR-18-525108), and the National
842 Institutes of Health (NIH) National Institute of General Medical Sciences (NIGMS) award
843 R01GM132753 to N.J.O.

844

845 **Author contributions:** D.D., M.L., P.G.B., A.L.E., and N.J.O. Conceived, designed, and
846 interpreted experiments. D.D., M.L., P.G.B., S.R., B.Z., E.M., D.A., and N.J.O., performed all
847 experiments, acquired and analyzed data. D.D. and N.J.O. wrote the manuscript. All authors read
848 the manuscript, provided comments, and approved the final version.

849

850 **Declaration of interests:** The authors declare no competing or financial interest.

851

852

853

REFERENCES

Abnave, P., Aboukhatwa, E., Kosaka, N., Thompson, J., Hill, M. A. and Aboobaker, A. A. (2017). Epithelial-mesenchymal transition transcription factors control pluripotent adult stem cell migration in vivo in planarians. *Development* **144**, 3440-3453.

Adee, S. (2018). Original Sin. *Bioelectricity* **1**, 10-11.

Aleem, I. S., Aleem, I., Evaniew, N., Busse, J. W., Yaszemski, M., Agarwal, A., Einhorn, T. and Bhandari, M. (2016). Efficacy of Electrical Stimulators for Bone Healing: A Meta-Analysis of Randomized Sham-Controlled Trials. *Scientific Reports* **6**, 31724.

Alexa, A. and Rahnenfuhrer, J. (2020). topGO: Enrichment Analysis for Gene Ontology. R package version 2.42.0.

Alexa, A., Rahnenfuhrer, J. and Lengauer, T. (2006). Improved scoring of functional groups from gene expression data by decorrelating GO graph structure. *Bioinformatics (Oxford, England)* **22**, 1600-7.

Amir, R. E., Van den Veyver, I. B., Wan, M., Tran, C. Q., Francke, U. and Zoghbi, H. Y. (1999). Rett syndrome is caused by mutations in X-linked MECP2, encoding methyl-CpG-binding protein 2. *Nat Genet* **23**, 185-8.

Antal, A., Alekseichuk, I., Bikson, M., Brockmöller, J., Brunoni, A. R., Chen, R., Cohen, L. G., Dowthwaite, G., Ellrich, J., Flöel, A. et al. (2017). Low intensity transcranial electric stimulation: Safety, ethical, legal regulatory and application guidelines. *Clinical Neurophysiology* **128**, 1774-1809.

Antal, A., Kriener, N., Lang, N., Boros, K. and Paulus, W. (2011). Cathodal transcranial direct current stimulation of the visual cortex in the prophylactic treatment of migraine. *Cephalalgia* **31**, 820-8.

Antal, A., Lang, N., Boros, K., Nitsche, M., Siebner, H. R. and Paulus, W. (2008). Homeostatic metaplasticity of the motor cortex is altered during headache-free intervals in migraine with aura. *Cereb Cortex* **18**, 2701-5.

Bahrami, S. and Drablos, F. (2016). Gene regulation in the immediate-early response process. *Adv Biol Regul* **62**, 37-49.

Baker, S. A., Chen, L., Wilkins, A. D., Yu, P., Lichtarge, O. and Zoghbi, H. Y. (2013). An AT-hook domain in MeCP2 determines the clinical course of Rett syndrome and related disorders. *Cell* **152**, 984-96.

Bardeen, C. R. and Baetjer, F. H. (1904). The inhibitive action of the Roentgen rays on regeneration in planarians. *J. Exp. Zool.* **1**, 191-195.

Barghouth, P. G., Thiruvalluvan, M., LeGro, M. and Oviedo, N. J. (2018). DNA damage and tissue repair: What we can learn from planaria. *Semin Cell Dev Biol*.

Barghouth, P. G., Thiruvalluvan, M., LeGro, M. and Oviedo, N. J. (2019). DNA damage and tissue repair: What we can learn from planaria. *Semin Cell Dev Biol* **87**, 145-159.

Bewernick, B. H., Kayser, S., Sturm, V. and Schlaepfer, T. E. (2012). Long-term effects of nucleus accumbens deep brain stimulation in treatment-resistant depression: evidence for sustained efficacy. *Neuropsychopharmacology* **37**, 1975-85.

Bikson, M., Inoue, M., Akiyama, H., Deans, J. K., Fox, J. E., Miyakawa, H. and Jefferys, J. G. (2004). Effects of uniform extracellular DC electric fields on excitability in rat hippocampal slices in vitro. *J Physiol* **557**, 175-90.

Boggio, P. S., Nunes, A., Rigonatti, S. P., Nitsche, M. A., Pascual-Leone, A. and Fregni, F. (2007). Repeated sessions of noninvasive brain DC stimulation is associated with motor function improvement in stroke patients. *Restor Neurol Neurosci* **25**, 123-9.

Boggio, P. S., Zaghi, S. and Fregni, F. (2009). Modulation of emotions associated with images of human pain using anodal transcranial direct current stimulation (tDCS). *Neuropsychologia* **47**, 212-7.

Boggio, P. S., Zaghi, S., Lopes, M. and Fregni, F. (2008). Modulatory effects of anodal transcranial direct current stimulation on perception and pain thresholds in healthy volunteers. *Eur J Neurol* **15**, 1124-30.

Bonar, N. A. and Petersen, C. P. (2017). Integrin suppresses neurogenesis and regulates brain tissue assembly in planarian regeneration. *Development* **144**, 784-794.

Bonner, W. M., Redon, C. E., Dickey, J. S., Nakamura, A. J., Sedelnikova, O. A., Solier, S. and Pommier, Y. (2008). GammaH2AX and cancer. *Nat Rev Cancer* **8**, 957-67.

Borckardt, J. J., Bikson, M., Frohman, H., Reeves, S. T., Datta, A., Bansal, V., Madan, A., Barth, K. and George, M. S. (2012). A pilot study of the tolerability and effects of high-definition transcranial direct current stimulation (HD-tDCS) on pain perception. *J Pain* **13**, 112-20.

Borgens, R. B., Blight, A. R. and McGinnis, M. E. (1987). Behavioral recovery induced by applied electric fields after spinal cord hemisection in guinea pig. *Science* **238**, 366-9.

Bresadola, M. (1998). Medicine and science in the life of Luigi Galvani (1737-1798). *Brain Res Bull* **46**, 367-80.

Brighton, C. T. (1981). Treatment of nonunion of the tibia with constant direct current (1980 Fitts Lecture, A.A.S.T.). *J Trauma* **21**, 189-95.

Brighton, C. T., Black, J., Friedenberg, Z. B., Esterhai, J. L., Day, L. J. and Connolly, J. F. (1981). A multicenter study of the treatment of non-union with constant direct current. *J Bone Joint Surg Am* **63**, 2-13.

Chahrour, M., Jung, S. Y., Shaw, C., Zhou, X., Wong, S. T., Qin, J. and Zoghbi, H. Y. (2008). MeCP2, a key contributor to neurological disease, activates and represses transcription. *Science* **320**, 1224-9.

Chaieb, L., Saiote, C., Paulus, W. and Antal, A. (2014). The Stimulated Brain. *PART II: IMPROVING FUNCTIONS IN THE TYPICAL BRAIN*, 181-205.

Chan, J. D., Zhang, D., Liu, X., Zarowiecki, M., Berriman, M. and Marchant, J. S. (2017). Utilizing the planarian voltage-gated ion channel transcriptome to resolve a role for a Ca(2+) channel in neuromuscular function and regeneration. *Biochim Biophys Acta Mol Cell Res* **1864**, 1036-1045.

Chang, H. F., Lee, Y. S., Tang, T. K. and Cheng, J. Y. (2016). Pulsed DC Electric Field-Induced Differentiation of Cortical Neural Precursor Cells. *PLoS One* **11**, e0158133.

Chrisman, S. D., Waite, C. B., Scoville, A. G. and Carnell, L. (2016). C. elegans Demonstrates Distinct Behaviors within a Fixed and Uniform Electric Field. *PLoS One* **11**, e0151320.

Coates McCall, I., Lau, C., Minielly, N. and Illes, J. (2019). Owning Ethical Innovation: Claims about Commercial Wearable Brain Technologies. *Neuron* **102**, 728-731.

Cohen, S. and Greenberg, M. E. (2008). Communication between the synapse and the nucleus in neuronal development, plasticity, and disease. *Annu Rev Cell Dev Biol* **24**, 183-209.

Cote, L. E., Simental, E. and Reddien, P. W. (2019). Muscle functions as a connective tissue and source of extracellular matrix in planarians. *Nature Communications* **10**, 1592.

Cullingford, T. E., Markou, T., Fuller, S. J., Giraldo, A., Pikkarainen, S., Zoumpoulidou, G., Alsafi, A., Ekere, C., Kemp, T. J., Dennis, J. L. et al. (2008). Temporal regulation of expression of immediate early and second phase transcripts by endothelin-1 in cardiomyocytes. *Genome Biology* **9**, R32.

Davidian, D., Ziman, B., Escobar, A. L. and Oviedo, N. J. (2020). Direct current electric stimulation alters the frequency and the distribution of mitotic cells in planarians. *Bioelectricity*.

de Sousa, N., Rodríguez-Esteban, G., Rojo-Laguna, J., Saló, E. and Adell, T. (2018). Hippo signaling controls cell cycle and restricts cell plasticity in planarians. *PLoS Biol* **16**.

Delaloye, S. and Holtzheimer, P. E. (2014). Deep brain stimulation in the treatment of depression. *Dialogues Clin Neurosci* **16**, 83-91.

Dragunow, M. and Robertson, H. A. (1987). Kindling stimulation induces c-fos protein(s) in granule cells of the rat dentate gyrus. *Nature* **329**, 441-2.

Eisenhoffer, G. T., Kang, H. and Alvarado, A. S. (2008a). Molecular Analysis of Stem Cells and Their Descendants during Cell Turnover and Regeneration in the Planarian Schmidtea mediterranea. *Cell Stem Cell* **3**, 327-339.

Eisenhoffer, G. T., Kang, H. and Sánchez Alvarado, A. (2008b). Molecular analysis of stem cells and their descendants during cell turnover and regeneration in the planarian Schmidtea mediterranea. *Cell Stem Cell* **3**, 327-39.

Elliott, C., Vijayakumar, V., Zink, W. and Hansen, R. (2007). National Instruments LabVIEW: A Programming Environment for Laboratory Automation and Measurement. *Journal of the Association for Laboratory Automation* **12**, 17-24.

Elliott, P. (2014). The Stimulated Brain. *PART I: THE BASIS*, 3-33.

Feng, J. F., Liu, J., Zhang, L., Jiang, J. Y., Russell, M., Lyeth, B. G., Nolta, J. A. and Zhao, M. (2017). Electrical Guidance of Human Stem Cells in the Rat Brain. *Stem Cell Reports* **9**, 177-189.

Fincher, C. T., Wurtzel, O., de Hoog, T., Kravarik, K. M. and Reddien, P. W. (2018). Cell type transcriptome atlas for the planarian Schmidtea mediterranea. *Science*.

Formento, E., Minassian, K., Wagner, F., Mignardot, J. B., Le Goff-Mignardot, C. G., Rowald, A., Bloch, J., Micera, S., Capogrosso, M. and Courtine, G. (2018). Electrical spinal cord stimulation must preserve proprioception to enable locomotion in humans with spinal cord injury. *Nat Neurosci* **21**, 1728-1741.

Forsthoefel, D. J., Waters, F. A. and Newmark, P. A. (2014). Generation of cell type-specific monoclonal antibodies for the planarian and optimization of sample processing for immunolabeling. *BMC Dev Biol* **14**, 45.

Gao, M., Wei, W., Li, M. M., Wu, Y. S., Ba, Z., Jin, K. X., Li, M. M., Liao, Y. Q., Adhikari, S., Chong, Z. et al. (2014). Ago2 facilitates Rad51 recruitment and DNA double-strand break repair by homologous recombination. *Cell Res* **24**, 532-41.

Gerovasili, V., Stefanidis, K., Vitzilaios, K., Karatzanos, E., Politis, P., Koroneos, A., Chatzimichail, A., Routsi, C., Roussos, C. and Nanas, S. (2009). Electrical muscle stimulation preserves the muscle mass of critically ill patients: a randomized study. *Crit Care* **13**, R161.

Graham, D. M., Huang, L., Robinson, K. R. and Messerli, M. A. (2013). Epidermal keratinocyte polarity and motility require Ca(2)(+) influx through TRPV1. *J Cell Sci* **126**, 4602-13.

Graupe, D., Khobragade, N., Tuninetti, D., Basu, I., Slavin, K. V. and Verhagen Metman, L. (2018). Who May Benefit From On-Demand Control of Deep Brain Stimulation? Noninvasive Evaluation of Parkinson Patients. *Neuromodulation*.

Greenberg, M. E., Ziff, E. B. and Greene, L. A. (1986). Stimulation of neuronal acetylcholine receptors induces rapid gene transcription. *Science* **234**, 80-3.

Greer, P. L. and Greenberg, M. E. (2008). From synapse to nucleus: calcium-dependent gene transcription in the control of synapse development and function. *Neuron* **59**, 846-60.

Griffin, M. and Bayat, A. (2011). Electrical stimulation in bone healing: critical analysis by evaluating levels of evidence. *Eplasty* **11**.

Grohme, M. A., Schloissnig, S., Rozanski, A., Pippel, M., Young, G. R., Winkler, S., Brandl, H., Henry, I., Dahl, A., Powell, S. et al. (2018). The genome of Schmidtea mediterranea and the evolution of core cellular mechanisms. *Nature* **554**, 56-61.

Guedelhoefer, O. C. t. and Sanchez Alvarado, A. (2012a). Amputation induces stem cell mobilization to sites of injury during planarian regeneration. *Development* **139**, 3510-20.

Guedelhoefer, O. C. t. and Sanchez Alvarado, A. (2012b). Planarian immobilization, partial irradiation, and tissue transplantation. *J Vis Exp*.

Guo, A., Song, B., Reid, B., Gu, Y., Forrester, J. V., Jahoda, C. A. and Zhao, M. (2010). Effects of physiological electric fields on migration of human dermal fibroblasts. *J Invest Dermatol* **130**, 2320-7.

Haaf, T., Raderschall, E., Reddy, G., Ward, D. C., Radding, C. M. and Golub, E. I. (1999). Sequestration of Mammalian Rad51-Recombination Protein into Micronuclei. *The Journal of Cell Biology* **144**, 11-20.

Hao, S., Tang, B., Wu, Z., Ure, K., Sun, Y., Tao, H., Gao, Y., Patel, A. J., Curry, D. J., Samaco, R. C. et al. (2015). Forniceal deep brain stimulation rescues hippocampal memory in Rett syndrome mice. *Nature* **526**, 430-4.

Herschman, H. R. (1991). Primary response genes induced by growth factors and tumor promoters. *Annu Rev Biochem* **60**, 281-319.

Holtzheimer, P. E., Kelley, M. E., Gross, R. E., Filkowski, M. M., Garlow, S. J., Barrocas, A., Wint, D., Craighead, M. C., Kozarsky, J., Chismar, R. et al. (2012). Subcallosal cingulate deep brain stimulation for treatment-resistant unipolar and bipolar depression. *Arch Gen Psychiatry* **69**, 150-8.

Huang, Y., Li, Y., Chen, J., Zhou, H. and Tan, S. (2015a). Electrical Stimulation Elicits Neural Stem Cells Activation: New Perspectives in CNS Repair. *Front Hum Neurosci* **9**, 586.

Huang, Y., Li, Y., Chen, J., Zhou, H. and Tan, S. (2015b). Electrical Stimulation Elicits Neural Stem Cells Activation: New Perspectives in CNS Repair. *Frontiers in Human Neuroscience* **9**, 586.

Isolani, M. E., Abril, J. F., Salo, E., Deri, P., Bianucci, A. M. and Batistoni, R. (2013). Planarians as a model to assess in vivo the role of matrix metalloproteinase genes during homeostasis and regeneration. *PLoS One* **8**, e55649.

Jaffe, L. F. (1981a). Control of development by steady ionic currents. *Fed Proc* **40**, 125-7.

Jaffe, L. F. (1981b). The role of ionic currents in establishing developmental pattern. *Philos Trans R Soc Lond B Biol Sci* **295**, 553-66.

Johnson, B. S., Zhao, Y. T., Fasolino, M., Lamonica, J. M., Kim, Y. J., Georgakilas, G., Wood, K. H., Bu, D., Cui, Y., Goffin, D. et al. (2017). Biotin tagging of MeCP2 in mice reveals contextual insights into the Rett syndrome transcriptome. *Nat Med* **23**, 1203-1214.

Kadosh, R. (2015). Modulating and enhancing cognition using brain stimulation: Science and fiction. *Journal of Cognitive Psychology* **27**, 141-163.

Kadosh, R., Soskic, S., Iuculano, T., Kanai, R. and Walsh, V. (2010). Modulating Neuronal Activity Produces Specific and Long-Lasting Changes in Numerical Competence. *Current Biology* **20**, 2016-2020.

Kandel, E. R. (2012). The molecular biology of memory: cAMP, PKA, CRE, CREB-1, CREB-2, and CPEB. *Mol Brain* **5**, 14.

Kim, I. V., Duncan, E. M., Ross, E. J., Gorbovytska, V., Nowotarski, S. H., Elliott, S. A., Sanchez Alvarado, A. and Kuhn, C. D. (2019). Planarians recruit piRNAs for mRNA turnover in adult stem cells. *Genes Dev* **33**, 1575-1590.

King, R. S. and Newmark, P. A. (2013). In situ hybridization protocol for enhanced detection of gene expression in the planarian Schmidtea mediterranea. *BMC Dev Biol* **13**, 8.

Kuzyk, P. R. and Schemitsch, E. H. (2009). The science of electrical stimulation therapy for fracture healing. *Indian Journal of Orthopaedics* **43**, 127-131.

Law, C. W., Chen, Y., Shi, W. and Smyth, G. K. (2014). voom: Precision weights unlock linear model analysis tools for RNA-seq read counts. *Genome Biology* **15**, R29.

Lei, K., Thi-Kim Vu, H., Mohan, R. D., McKinney, S. A., Seidel, C. W., Alexander, R., Gotting, K., Workman, J. L. and Sanchez Alvarado, A. (2016). Egf Signaling Directs Neoblast Repopulation by Regulating Asymmetric Cell Division in Planarians. *Dev Cell* **38**, 413-29.

Levin, M. (2007). Large-scale biophysics: ion flows and regeneration. *Trends Cell Biol* **17**, 261-70.

Levin, M. (2014). Molecular bioelectricity: how endogenous voltage potentials control cell behavior and instruct pattern regulation in vivo. *Mol Biol Cell* **25**, 3835-50.

Liao, Y., Smyth, G. K. and Shi, W. (2013). The Subread aligner: fast, accurate and scalable read mapping by seed-and-vote. *Nucleic Acids Res* **41**, e108.

Liu, R., Holik, A. Z., Su, S., Jansz, N., Chen, K., Leong, H. S., Blewitt, M. E., Asselin-Labat, M. L., Smyth, G. K. and Ritchie, M. E. (2015). Why weight? Modelling sample and observational level variability improves power in RNA-seq analyses. *Nucleic Acids Res* **43**, e97.

Lu, H., Ash, R. T., He, L., Kee, S. E., Wang, W., Yu, D., Hao, S., Meng, X., Ure, K., Ito-Ishida, A. et al. (2016). Loss and Gain of MeCP2 Cause Similar Hippocampal Circuit Dysfunction that Is Rescued by Deep Brain Stimulation in a Rett Syndrome Mouse Model. *Neuron* **91**, 739-747.

Ma, L. and Yan, X. (2014). Examining the nonparametric effect of drivers' age in rear-end accidents through an additive logistic regression model. *Accid Anal Prev* **67**, 129-36.

Marchant, J. S. (2019). Ca(2+) Signaling and Regeneration. *Cold Spring Harb Perspect Biol*.

Marsh, G. and Beams, H. W. (1952). Electrical control of morphogenesis in regenerating Dugesia tigrina. I. Relation of axial polarity to field strength. *J Cell Physiol* **39**, 191-213.

Marti, T. M., Hefner, E., Feeney, L., Natale, V. and Cleaver, J. E. (2006). H2AX phosphorylation within the G1 phase after UV irradiation depends on nucleotide excision repair and not DNA double-strand breaks. *Proc Natl Acad Sci U S A* **103**, 9891-6.

Mayberg, H. S., Lozano, A. M., Voon, V., McNeely, H. E., Seminowicz, D., Hamani, C., Schwalb, J. M. and Kennedy, S. H. (2005). Deep brain stimulation for treatment-resistant depression. *Neuron* **45**, 651-60.

McCaig, C. D., Rajnicek, A. M., Song, B. and Zhao, M. (2005). Controlling cell behavior electrically: current views and future potential. *Physiol Rev* **85**, 943-78.

McLaughlin, K. A. and Levin, M. (2018). Bioelectric signaling in regeneration: Mechanisms of ionic controls of growth and form. *Dev Biol* **433**, 177-189.

Miocinovic, S., Somayajula, S., Chitnis, S. and Vitek, J. L. (2013). History, applications, and mechanisms of deep brain stimulation. *JAMA Neurol* **70**, 163-71.

Mohammed, A., Bayford, R. and Demosthenous, A. (2018). Toward adaptive deep brain stimulation in Parkinson's disease: a review. *Neurodegener Dis Manag* **8**, 115-136.

Molinaro, A. M., Lindsay-Mosher, N. and Pearson, B. J. (2021). Identification of TOR-responsive slow-cycling neoblasts in planarians. *EMBO Rep* **22**, e50292.

Molinaro, A. M. and Pearson, B. J. (2016). In silico lineage tracing through single cell transcriptomics identifies a neural stem cell population in planarians. *Genome Biol* **17**, 87.

Moreno-Duarte, I., Gebodh, N., Schestatsky, P., Guleyupoglu, B., Reato, D., Bikson, M. and Fregni, F. (2014). The Stimulated Brain. *PART I: THE BASIS*, 35-59.

Morgan, J. I. and Curran, T. (1991). Stimulus-transcription coupling in the nervous system: involvement of the inducible proto-oncogenes fos and jun. *Annu Rev Neurosci* **14**, 421-51.

Mylius, V., Borckardt, J. J. and Lefaucheur, J. P. (2012). Noninvasive cortical modulation of experimental pain. *Pain* **153**, 1350-63.

Nelson, J., McKinley, R. A., Phillips, C., McIntire, L., Goodyear, C., Kreiner, A. and Monforton, L. (2016). The Effects of Transcranial Direct Current Stimulation (tDCS) on Multitasking Throughput Capacity. *Frontiers in Human Neuroscience* **10**, 589.

Newmark, P. and Sánchez Alvarado, A. (2000). Bromodeoxyuridine specifically labels the regenerative stem cells of planarians. *Dev. Biol.* **220**, 142-53.

Niemann, M., Schneider, G. H., Kuhn, A., Vajkoczy, P. and Faust, K. (2017). Longevity of Implantable Pulse Generators in Bilateral Deep Brain Stimulation for Movement Disorders. *Neuromodulation*.

Nogi, T., Zhang, D., Chan, J. D. and Marchant, J. S. (2009). A novel biological activity of praziquantel requiring voltage-operated Ca2+ channel beta subunits: subversion of flatworm regenerative polarity. *PLoS Negl Trop Dis* **3**, e464.

Nuccitelli, R. (2003). A role for endogenous electric fields in wound healing. *Curr Top Dev Biol* **58**, 1-26.

Nuccitelli, R. and Jaffe, L. F. (1974). Spontaneous current pulses through developing fucoid eggs. *Proc Natl Acad Sci U S A* **71**, 4855-9.

Ogawa, N., Oku, H., Hashimoto, K. and Ishikawa, M. (2006). A physical model for galvanotaxis of Paramecium cell. *J Theor Biol* **242**, 314-28.

Organization, W. H. (2018). Depression.

Oviedo, N. J., Nicolas, C., Adams, D. S. and Levin, M. (2008a). Gene knockdown in planarians using RNAi interference. *Cold Spring Harb Protocols* **3**, 902-906.

Oviedo, N. J., Nicolas, C. L., Adams, D. S. and Levin, M. (2008b). Establishing and maintaining a colony of planarians. *CSH Protoc* **2008**, pdb prot5053.

Oviedo, N. J., Pearson, B. J., Levin, M. and Sanchez Alvarado, A. (2008c). Planarian PTEN homologs regulate stem cells and regeneration through TOR signaling. *Disease Models and Mechanisms* **1**, 131-143.

Palakodeti, D., Smielewska, M., Lu, Y.-C., Yeo, G. W. and Graveley, B. R. (2008a). The PIWI proteins SMEDWI-2 and SMEDWI-3 are required for stem cell function and piRNA expression in planarians. *RNA (New York, N.Y.)* **14**, 1174-1186.

Palakodeti, D., Smielewska, M., Lu, Y. C., Yeo, G. W. and Graveley, B. R. (2008b). The PIWI proteins SMEDWI-2 and SMEDWI-3 are required for stem cell function and piRNA expression in planarians. *RNA (New York, N.Y.)* **14**, 1174-86.

Peiris, T. H., Garcia-Ojeda, M. E. and Oviedo, N. J. (2016a). Alternative flow cytometry strategies to analyze stem cells and cell death in planarians. *Regeneration (Oxf)* **3**, 123-35.

Peiris, T. H., Ramirez, D., Barghouth, P. G., Ofoha, U., Davidian, D., Weckerle, F. and Oviedo, N. J. (2016b). Regional signals in the planarian body guide stem cell fate in the presence of genomic instability. *Development* **143**, 1697-709.

Pellettieri, J., Fitzgerald, P., Watanabe, S., Mancuso, J., Green, D. R. and Sanchez Alvarado, A. (2010). Cell death and tissue remodeling in planarian regeneration. *Dev Biol* **338**, 76-85.

Phipson, B., Lee, S., Majewski, I. J., Alexander, W. S. and Smyth, G. K. (2016). Robust Hyperparameter Estimation Protects against Hypervariable Genes and Improves Power to Detect Differential Expression. *Ann Appl Stat* **10**, 946-963.

Plass, M., Solana, J., Wolf, A. F., Ayoub, S., Misios, A., Glažar, P., Obermayer, B., Theis, F. J., Kocks, C. and Rajewsky, N. (2018). Cell type atlas and lineage tree of a whole complex animal by single-cell transcriptomics. *Science*.

Pohodich, A. E., Yalamanchili, H., Raman, A. T., Wan, Y. W., Gundry, M., Hao, S., Jin, H., Tang, J., Liu, Z. and Zoghbi, H. Y. (2018). Forniceal deep brain stimulation induces gene expression and splicing changes that promote neurogenesis and plasticity. *Elife* **7**.

Qi, Y., Zhang, Y., Baller, J. A. and Voytas, D. F. (2016). Histone H2AX and the small RNA pathway modulate both non-homologous end-joining and homologous recombination in plants. *Mutat Res* **783**, 9-14.

Reddien, P. W. (2018). The Cellular and Molecular Basis for Planarian Regeneration. *Cell* **175**, 327-345.

Reddien, P. W., Oviedo, N. J., Jennings, J. R., Jenkin, J. C. and Sánchez Alvarado, A. (2005). SMEDWI-2 is a PIWI-like protein that regulates planarian stem cells. *Science* **310**, 1327-1330.

Rink, J. C. (2018). Stem Cells, Patterning and Regeneration in Planarians: Self-Organization at the Organismal Scale. *Methods Mol Biol* **1774**, 57-172.

Ritchie, M. E., Phipson, B., Wu, D., Hu, Y., Law, C. W., Shi, W. and Smyth, G. K. (2015). limma powers differential expression analyses for RNA-sequencing and microarray studies. *Nucleic Acids Res* **43**, e47.

Robb, S. M., Gotting, K., Ross, E. and Sanchez Alvarado, A. (2015). SmedGD 2.0: The Schmidtea mediterranea genome database. *Genesis* **53**, 535-46.

Saha, R. N. and Dudek, S. M. (2013). Splitting hares and tortoises: a classification of neuronal immediate early gene transcription based on poised RNA polymerase II. *Neuroscience* **247**, 175-81.

Saha, R. N., Wissink, E. M., Bailey, E. R., Zhao, M., Fargo, D. C., Hwang, J. Y., Daigle, K. R., Fenn, J. D., Adelman, K. and Dudek, S. M. (2011). Rapid activity-induced transcription of Arc and other IEGs relies on poised RNA polymerase II. *Nat Neurosci* **14**, 848-56.

Salo, E. and Baguna, J. (1985). Cell movement in intact and regenerating planarians. Quantitation using chromosomal, nuclear and cytoplasmic markers. *J Embryol Exp Morphol* **89**, 57-70.

Sandmann, T., Vogg, M. C., Owlarn, S., Boutros, M. and Bartscherer, K. (2011). The head-regeneration transcriptome of the planarian Schmidtea mediterranea. *Genome Biology* **12**, R76.

Sarkar, A. and Kadosh, R. (2016). Development of Mathematical Cognition. *Part I: Neural substrates*, 245-296.

Scimone, M. L., Atabay, K. D., Fincher, C. T., Bonneau, A. R., Li, D. J. and Reddien, P. W. (2020). Muscle and neuronal guidepost-like cells facilitate planarian visual system regeneration. *Science* **368**.

Scimone, M. L., Cote, L. E. and Reddien, P. W. (2017). Orthogonal muscle fibres have different instructive roles in planarian regeneration. *Nature* **551**, 623-628.

Seebeck, F., Marz, M., Meyer, A. W., Reuter, H., Vogg, M. C., Stehling, M., Mildner, K., Zeuschner, D., Rabert, F. and Bartscherer, K. (2017). Integrins are required for tissue organization and restriction of neurogenesis in regenerating planarians. *Development* **144**, 795-807.

Smyth, G. K. and Speed, T. (2003). Normalization of cDNA microarray data. *Methods* **31**, 265-73.

Snowball, A., Tachtsidis, I., Popescu, T., Thompson, J., Delazer, M., Zamarian, L., Zhu, T. and Cohen Kadosh, R. (2013). Long-Term Enhancement of Brain Function and Cognition Using Cognitive Training and Brain Stimulation. *Current Biology* **23**, 987-992.

Stump, R. F. and Robinson, K. R. (1983). Xenopus neural crest cell migration in an applied electrical field. *J Cell Biol* **97**, 1226-33.

Sugino, K., Hempel, C. M., Okaty, B. W., Arnson, H. A., Kato, S., Dani, V. S. and Nelson, S. B. (2014). Cell-type-specific repression by methyl-CpG-binding protein 2 is biased toward long genes. *J Neurosci* **34**, 12877-83.

Thiruvalluvan, M., Barghouth, P. G., Tsur, A., Broday, L. and Oviedo, N. J. (2018). SUMOylation controls stem cell proliferation and regional cell death through Hedgehog signaling in planarians. *Cell Mol Life Sci* **75**, 1285-1301.

Tortella, G., Casati, R., Aparicio, L. V., Mantovani, A., Senco, N., D'Urso, G., Brunelin, J., Guarienti, F., Selingardi, P. M., Muszkat, D. et al. (2015). Transcranial direct current stimulation in psychiatric disorders. *World J Psychiatry* **5**, 88-102.

Tu, K. C., Cheng, L.-C., T K Vu, H., Lange, J. J., McKinney, S. A., Seidel, C. W. and Sánchez Alvarado, A. (2015a). Egr-5 is a post-mitotic regulator of planarian epidermal differentiation. *eLife* **4**, e10501.

Tu, K. C., Cheng, L. C., H, T. K. V., Lange, J. J., McKinney, S. A., Seidel, C. W. and Sanchez Alvarado, A. (2015b). Egr-5 is a post-mitotic regulator of planarian epidermal differentiation. *Elife* **4**, e10501.

Tullai, J. W., Schaffer, M. E., Mullenbrock, S., Sholder, G., Kasif, S. and Cooper, G. M. (2007). Immediate-early and delayed primary response genes are distinct in function and genomic architecture. *J Biol Chem* **282**, 23981-95.

Uhlitz, F., Sieber, A., Wyler, E., Fritsche-Guenther, R., Meisig, J., Landthaler, M., Klinger, B. and Bluthgen, N. (2017). An immediate-late gene expression module decodes ERK signal duration. *Mol Syst Biol* **13**, 928.

van Wolfswinkel, J. C., Wagner, D. E. and Reddien, P. W. (2014a). Single-cell analysis reveals functionally distinct classes within the planarian stem cell compartment. *Cell Stem Cell* **15**, 326-339.

van Wolfswinkel, J. C., Wagner, D. E. and Reddien, P. W. (2014b). Single-cell analysis reveals functionally distinct classes within the planarian stem cell compartment. *Cell Stem Cell* **15**, 326-39.

Velarde, O. M., Mato, G. and Dellavale, D. (2017). Mechanisms for pattern specificity of deep-brain stimulation in Parkinson's disease. *PLoS One* **12**, e0182884.

Wagner, D. E., Ho, J. J. and Reddien, P. W. (2012). Genetic regulators of a pluripotent adult stem cell system in planarians identified by RNAi and clonal analysis. *Cell Stem Cell* **10**, 299-311.

Wagner, D. E., Wang, I. E. and Reddien, P. W. (2011). Clonogenic neoblasts are pluripotent adult stem cells that underlie planarian regeneration. *Science* **332**, 811-6.

Wagner, F. B., Mignardot, J. B., Le Goff-Mignardot, C. G., Demesmaeker, R., Komi, S., Capogrosso, M., Rowald, A., Seanez, I., Caban, M., Pirondini, E. et al. (2018). Targeted neurotechnology restores walking in humans with spinal cord injury. *Nature* **563**, 65-71.

Wei, W., Ba, Z., Gao, M., Wu, Y., Ma, Y., Amiard, S., White, C. I., Rendtlew Danielsen, J. M., Yang, Y. G. and Qi, Y. (2012). A role for small RNAs in DNA double-strand break repair. *Cell* **149**, 101-12.

West, A. E. and Greenberg, M. E. (2011). Neuronal activity-regulated gene transcription in synapse development and cognitive function. *Cold Spring Harb Perspect Biol* **3**.

Wexler, A. and Reiner, P. B. (2019). Oversight of direct-to-consumer neurotechnologies. *Science* **363**, 234-235.

Wurzman, R., Hamilton, R. H., Pascual-Leone, A. and Fox, M. D. (2016). An open letter concerning do-it-yourself users of transcranial direct current stimulation. *Ann Neurol* **80**, 1-4.

Yan, X., Liu, J., Huang, J., Huang, M., He, F., Ye, Z., Xiao, W., Hu, X. and Luo, Z. (2014). Electrical stimulation induces calcium-dependent neurite outgrowth and immediate early genes expressions of dorsal root ganglion neurons. *Neurochem Res* **39**, 129-41.

Zeng, A., Li, H., Guo, L., Gao, X., McKinney, S., Wang, Y., Yu, Z., Park, J., Semerad, C., Ross, E. et al. (2018a). Prospectively Isolated Tetraspanin + Neoblasts Are Adult Pluripotent Stem Cells Underlying Planaria Regeneration. *Cell* **173**, 1593-1608.e20.

Zeng, A., Li, H., Guo, L., Gao, X., McKinney, S., Wang, Y., Yu, Z., Park, J., Semerad, C., Ross, E. et al. (2018b). Prospectively Isolated Tetraspanin(+) Neoblasts Are Adult Pluripotent Stem Cells Underlying Planaria Regeneration. *Cell* **173**, 1593-1608 e20.

Zhao, M., Song, B., Pu, J., Wada, T., Reid, B., Tai, G., Wang, F., Guo, A., Walczysko, P., Gu, Y. et al. (2006). Electrical signals control wound healing through phosphatidylinositol-3-OH kinase-gamma and PTEN. *Nature* **442**, 457-60.

Zhu, S. J. and Pearson, B. J. (2016). (Neo)blast from the past: new insights into planarian stem cell lineages. *Curr Opin Genet Dev* **40**, 74-80.

Zhuang, H., Wang, W., Seldes, R. M., Tahernia, A. D., Fan, H. and Brighton, C. T. (1997). Electrical stimulation induces the level of TGF-beta1 mRNA in osteoblastic cells by a mechanism involving calcium/calmodulin pathway. *Biochem Biophys Res Commun* **237**, 225-9.

Figure Legends

Fig. 1. Schematic summary of planarian immobilization and pDCS setup. (A), Schematic representation of planarian immobilization. (B), Illustration of current-clamp circuit created by pDCS electrodes and planarian. (C), Amplified schematic representation of planarian tissues showing electrode placement and op-amps used to quantify current passing through the 100MΩ current clamp.

Fig. 2. pDCS triggers a transcriptional response and cell cycle in γ-irradiated host tissues. (A) Whole-mount *in situ* hybridization (WISH) showing *piwi-1*$^{+}$ signal in both wild-type (WT) and γ-irradiated (γ-irr, 60Gy) planarian (n=10/10). (B) Schematic depicting transplantation procedure using WT donor and irradiated host planarian with subsequent exposure to DCS. (C) WISH of *piwi-1* gene expression after four days post-transplant in both sham (control, n=10/10) and animals subjected to 60min pDCS (n=12/15). The insets in the lower portion of the image represent magnification of the distal part of the animal –tail-, *piwi-1* signal is indicated with arrows in animals subjected to pDCS. *(D) piwi-1* gene expression levels as determined by qPCR (pool of six animals/replicate and three biological replicates). (E-F) RNA-seq data collected from the host-tail tissue of sham and animals subjected to 60 mins pDCS (data was collected by pooling tails from four independently treated pDCS or sham planaria across three independent experimental trials). Gene expression heatmaps display differentially expressed transcripts (FDR<0.05) as averaged $\log_2$CPM Z-scores. (E) Heatmap representation of RNA-seq data displays differentially expressed neoblast subclass populations using the classical neoblast classification from van Wolfswinkel et al., 2014b; Wagner et al., 2012. (F) RNA-seq heatmap displays the neoblast subpopulations and their respective lineages based on recent neoblast

classification (Zeng et al., 2018b). (G) *cyclin-B* gene expression levels obtained with qPCR from tail fragments in both the sham and 60min pDCS (pool of six animals/replicate and three biological replicates). (H) RNA-seq heatmap displaying differentially expressed genes commonly associated with cell cycle regulation. (I) Whole-mount immunostaining with anti-H3P antibody (green dots) showing $H3P^{+}$ cells inside and outside of the transplant. Notice $H3P^{+}$ cells in the experimental group far away from the transplanted tissue (white arrows) following 6hrs pDCS compared to sham control (n=10/15). Dotted yellow circle: transplanted tissue (J) Magnified images around the transplanted tissue for both sham and pDCS after 6 hours of treatment (red and yellow arrows indicate mitotic cells in the anterior and posterior to the transplant -pink dotted line). (K) Average of $H3P^{+}$ cells in sham and the experimental groups after 6 hours of pDCS. pDCS experiments were executed with positive pole to the anterior and negative to the posterior for 60 minutes. Data represented as mean ± SEM. Students *t*-test: ****$P \leq 0.0001$. Scale bars, 500µm.

Fig. 3. Lethally irradiated host tissue is the main source of pDCS-induced neoblast transcription (A) Schematic representation depicting different regions of planarians subjected to tissue transplants from wild-type animals. (B-C) Gene expression levels of genes associated with cellular migration in planarians (*Snail-1*, *Snail-2*, *Zeb-1*, *ß1-integrin)*. The tissues used for each experiment were trunk (B) and tail (C) from the sham and pDCS-treated for 60 mins and the gene expression was measured with qPCR. (D, F, H) Depicts experimental design transplanting tissue from different donors and hosts to which tail fragments were processed to measure gene-level expression after four days of transplant. (D) *piwi-1(RNAi)* tissue into a lethally irradiated host, (F) transplant WT tissue into a *piwi-1(RNAi)* host, and (H) transplant γ-irr tissue into a γ-irr

host. (E, G, I) levels of gene expression from tissues obtained from sham and planarian subjected to 60 mins pDCS. The gene expression levels involved markers for diverse neoblast populations (*piwi-1*, *soxP-2*, *fgfr-1*, *egr-1*, *hnf-4*, *nkx2.2*, and *inx-13.* Pan neoblast (pNb), clonogenic neoblast (cNb), neoblast (Nb). Data represented as mean ± SEM. All gene expression experiments were obtained from three biological replicates consisting of four-pooled samples per replicate. The polarity of the electric field was positive pole to the anterior and negative to the posterior for 60 minutes. Statistical significance: multiple comparison one-way ANOVA: $*P \leq 0.05$, $**P \leq 0.01$, $***P \leq 0.001$, $****P \leq 0.0001$.

Fig. 4. pDCS enhances DNA damage response, reestablish DNA integrity and decreases cell death within γ-irradiated tissues. (A, B) Dissociated cells isolated from tail fragments were immunostained with anti-γH2AX and anti-RAD51 to visualize nuclear (DAPI) vs. cytoplasmic localization in sham and animals subjected to 60min pDCS. Nuclear γH2AX includes four classes of the nuclear signal as displayed in the left of (A) and previously described (Barghouth et al., 2018; Thiruvalluvan et al., 2018). The RAD51 signal was classified based on their localization with respect to DAPI as shown in in the left side of (B). Single-cell extract staining, experiments consisted of five pooled tail fragments and three biological replicates. (C) DNA integrity was measured with the COMET assay (mean tail length) using cells isolated from the host tail fragment in sham and worms subjected to 60min pDCS (n=12 each). (D,E,H) RNA-seq data obtained from tail fragments of sham and 60min pDCS tissue explants (data was collected by pooling tails from four independently treated pDCS or sham planaria across three independent experimental trials). Gene expression heatmaps display differentially expressed transcripts (FDR<0.05) as averaged $\log_2$CPM Z-scores for putative DNA damage regulators (D), DNA

repair regulators (E), and cell death regulators (H). (F) FACS analysis showing the distribution of live, pre-apoptotic, apoptotic, and necrotic cells using Annexin V in sham and 60min pDCS. The data includes four pooled tail fragments and three biological replicates. (G) Single-cell immunostaining using anti-caspase-3^{+} to denote three possible staining (active, pro-caspase and no caspase images on the left side of (H)). Caspase immunostaining was obtained from five pooled tail fragments and three biological replicates. Data represented as mean ± SEM obtained from experiments independently repeated at least three times. The polarity of the electric field was positive pole to the anterior and negative to the posterior for 60 minutes. Statistical significance: (A-C) Students *t*-test; (F,G) multiple comparison one-way ANOVA: $*P \leq 0.05$, $**P \leq 0.01$, $****P \leq 0.0001$.

Fig. 5. pDCS induces a rapid transcriptional response. (A, B) *piwi-1* gene expression with (A) whole-mount *in situ* hybridization and (B) qPCR at 15, 30, and 45 min of pDCS compared to the sham group. (A) lower-left corner shows the body image of lethally irradiated (60 Gy) animals four days post-transplant tissue from wildtype. The inset denotes the amplified tail section (sham = 10/10, 15min pDCS = 8/10, 30min pDCS = 9/13, 45min pDCS = 10/14). qPCR data represented as mean ± SEM obtained from triplicates consisting of five pooled samples per experiment and repeated two times. (C) Gene expression heatmap of neoblast markers from tail tissues explants, measured by qPCR. Shown are $\log_2$FC with column scaled Z-score (data is from six pooled tail fragments/replicates and three biological replicates). (D-F) RNA-seq data collected from tail tissue explants of irradiated and control animals (data was collected by pooling tails from four independently treated pDCS or sham planaria across three independent experimental trials) exposed to 60 min of pDCS. Gene expression heatmaps display differentially

expressed transcripts (FDR<0.05) as averaged log_2CPM Z-scores. (D) differentially expressed classic neoblast subclass populations based on reference (van Wolfswinkel et al., 2014b; Wagner et al., 2012). (E) differentially expressed neoblast subpopulations and their respective lineages based on reference (Zeng et al., 2018b). differentially expressed immediate-early gene putative homologs. The polarity of the electric field is denoted with a positive pole to the anterior and negative to the posterior for 60 minutes. Statistical significance: multiple comparison one-way ANOVA: ****$P \leq 0.0001$. Scale bars, 500µm.

Fig. 6. Ca^{2+} signaling mediates pDCS-induced ectopic expression of *piwi-1*. (A) Double fluorescent *in situ* hybridizations (FISH) were performed on sagittal cross-sections of sham and experimental group (n=six each). (B) Venn diagrams show percentage of *agat-1*$^+$ cell population expressing *piwi-1*$^+$ (left) or *piwi-1*$^+$ cells expressing *agat-1*$^+$ (right). (C) The average number of *piwi-1*$^+$ and *agat-1*$^+$. (D, E) Double FISH performed on sagittal cross-sections following 24hr soak with 5µM nicardipine or 60min incubation with 100µm EGTA [final concentration] (n=six each). (F-G) Venn diagrams show percentage of *agat-1*$^+$ cell population expressing *piwi-1*$^+$ (left) or *piwi-1*$^+$ cells expressing *agat-1*$^+$ (right) planarian exposed to 5µM nicardipine or 100µM EGTA. (J) Bar graph displays the average number of *piwi-1*$^+$ and *agat-1*$^+$ within each inhibition group. (K-L) Gene expression levels of neoblast markers *piwi-1*, *soxP2*, *fgfr1*, *egr1, hnf4, nkx2.2, and inx-13* using qPCR following 24hr 5µM nicardipine soak and 100 µM EGTA (data is from five pooled tail fragments/replicates and three biological replicates). All cases involve isolated tail tissue and pDCS for 15 min in the experimental group. Data represented as mean ± SEM. Pan neoblast (pNb), clonogenic neoblast (cNb), neoblast (Nb). The polarity of the electric field is denoted with a positive pole to the anterior and negative to the posterior for 60 minutes.

Statistical significance: (C) Students *t*-test; (F) Kolmogorov-Smirnov test, KS< 0.05 (I, K-L) multiple comparison one-way ANOVA: $^{**}P \leq 0.01$, $^{***}P \leq 0.001$, $^{****}P \leq 0.0001$. Scale bars, 100μm.

Fig. 7. Schematic summary of pDCS-induced effects. (A) pDCS-mediated effects in lethally γ-irradiated host tissue (gray cells) require engrafted neoblasts (colored cells, gray arrows). (B) Proposed cellular effects responsible for observed pDCS-induced transcriptional activation. Transcription sensitive to (1) Ca^{2+} influx through L-type Ca_v and subsequent (2) Ca^{2+} release from intracellular stores (i.e., endoplasmic reticulum) leading to (3) Ca^{2+}-mediated transcription and (4) expression of pDCS-induced genes. The ectopic overlapping expression of *agat-1*$^{+}$ populations with *piwi-1* suggests enhanced plasticity of transcriptional programs within the lethally γ-irradiated host tissue. ER=Endoplasmic Reticulum. (C) pDCS activates rapid transcription of genes associated with neoblast populations in lethally γ-irradiated host tissue.

Supplemental Information

Fig. S1. pDCS effects on mitotic activity and transcriptional response in tail transplanted tissues. (A) Immunostaining with anti-H3P antibody (green dots) representing three scenarios where pDCS was able to induce low or no change, moderate and robust number of mitotic cells exiting the transplant after 6hrs pDCS. Number of animals for each condition are included at the bottom of each image. (B**)** Illustration of current-clamp circuit created by pDCS electrodes and posterior transplanted planarian. (C) WISH addressing *piwi-1* gene expression of 60-minute pDCS. Tissue transplants involved transplant from WT into a γ-irr (60 Gy) host. Scale bars, 500μm.

Fig. S2. pDCS treatment amplifies DNA replication regulators. Heatmap showing significantly differentially expressed transcripts involved in DNA replication. RNA-seq data collected from tail tissue explants of sham and exposed to 60 min of pDCS (data was collected by pooling tails from four independently treated pDCS or sham planaria across three independent experimental trials). Tissue transplants involved transplant from WT into a γ-irr (60 Gy) host. Gene expression heatmaps display differentially expressed transcripts (FDR<0.05) as averaged $\log_2$CPM Z-scores.

Fig. S3. pDCS treatment increases the transcriptional activity of DNA repair, damage, and replication pathways. (A) Heatmaps showing significantly differentially expressed transcripts involved in DNA repair, (B) DNA damage, and, (C) DNA replication. RNA-seq data collected from tail tissue explants of sham and exposed to 60 min of pDCS (data was collected by pooling tails from 4 independently treated pDCS or sham planaria across 3 independent experimental

trials). Tissue transplants involved transplant from WT into a γ-irr (60 Gy) host. Gene expression heatmaps display differentially expressed transcripts (FDR<0.05) as averaged log_2CPM Z-scores.

Fig. S4. pDCS triggers transcription of immediate early genes. List of previously published and characterized immediate early genes (IEG) from Cullingford et al., 2008; Tullai et al., 2007; Uhlitz et al., 2017. Each IEG is listed with its full name and Ensembl gene ID. Gene names highlighted in red represent planarian differentially expressed putative IEG homologs to vertebrate counterpart.

Fig. S5. Treatment with dihydropyridines blocks pDCS effects. (A) Schematic showing WT donor/γ-irr host transplanted planarian subjected to 60min pDCS with 24hr 5μM nicardipine soak. Tail tissue was isolated and gene expression for (B) *piwi-1*, *soxP-2*, *fgfr-1*, *egr-1*, *hnf-4*, *nkx2.2*, and *inx-13* as well as (C) DDR genes: *MRE11, Ku70,* and *Rad51* measured by qRT-PCR (n=12, 3 biological replicates). (D) Double FISH was performed on sagittal cross-sections of sham control planarian and planarian exposed to 15min pDCS following 24hr 5μM nifedipine incubation (n=6). (E) Venn diagrams show percentage of *agat-1*$^+$ cell population expressing *piwi-1*$^+$ (left) or *piwi-1*$^+$ cells expressing *agat-1*$^+$ (right). (F) The average number of piwi-1$^+$ cells and agat-1$^+$ cells within tail tissue following 15min pDCS vs. sham planarian per section. (G) Gene expression levels of neoblast markers following 24hr 5μM nifedipine soak measured by qRT-PCR within 15min pDCS compared to the sham group (n=12, three biological replicates). (H) Heatmaps showing significantly differentially expressed transcripts involved in calcium signaling pathways for planarians treated with 15-minutes and 60-minutes pDCS treatment.

RNA-seq data collected from tail tissue explants of irradiated and control animals (data was collected by pooling tails from four independently treated pDCS or sham planaria across three independent experimental trials). Gene expression heatmaps display differentially expressed transcripts (FDR<0.05) as averaged log_2CPM Z-scores. Data represented as mean ± SEM. Statistical significance: (B, C, G) multiple comparison one-way ANOVA; (F) Students *t*-test: $^{**}P \leq 0.01$, $^{***}P \leq 0.001$, $^{****}P \leq 0.0001$. Scale bars, 100μm.

Fig. S6. Single-cell transcriptomic analysis displays an extensive spread enrichment of voltage-gated calcium channel alpha1S subunit in planarian tissues. (A) Single-cell distribution of L-type Ca_v alpha 1S subunit transcript (dd_smed_v4_8899_0_1) taken from *Planarian digiworm* database (Fincher et al., 2018). (B) Graphical key depicting localization for cell populations. (C) Listed cluster enrichment of L-type Ca_v alpha 1S subunit transcript showing high expression in neural, muscle, parenchymal, epidermal, and cathepsin+ cells.

Supplemental File 1. Differentially expressed transcripts and associated data for molecular pathway heatmaps. RNA-seq data showing differentially expressed transcripts for the 15 and 60 minutes timepoints and the associated BLAST data for *Homo sapiens* orthologs. Lists for cell cycle, DNA damage, DNA repair, DNA replication, and cell death molecular pathways are in the associated tabs of the excel workbook. All transcripts are expressed below the 5% level (B&H FDR<0.05) as averaged log_2CPM Z-scores.

Supplemental File 2. Enriched biological processes, cellular components, and molecular functions after applied pDCS. Gene set enrichment analysis of RNA-seq data collected from

the posterior regions of sham and planarians treated with 15 and 60 minutes of pDCS. Tissue transplants involved transplant from WT into a γ-irr (60 Gy) host. Tables plot the most significantly enriched Biological Processes, Cellular Components, and Molecular Functions. RNA-seq data collected from tail tissue explants of irradiated and sham animals (data was collected by pooling tails from four independently treated pDCS or sham planaria across three independent experimental trials). Kolmogorov-Smirnov test, KS< 0.05.

Supplemental File 3. Differentially expressed transcripts and associated data for NBSC and IEG heatmaps. RNA-seq data showing differentially expressed transcripts for the 15 and 60 minutes timepoints and the associated BLAST data for transcript orthologs. Lists for NBSC (Reddien, 2018; Rink, 2018; Zeng et al., 2018b; Zhu and Pearson, 2016) and IEGs are in the associated tabs of the excel workbook. All transcripts are expressed below the 5% level (B&H FDR<0.05) as averaged $\log_2$CPM Z-scores.

Supplemental File 4. RNA-seq analysis statistical results for all transcripts. RNA-seq analysis statistical results the 15 and 60 minutes timepoints. Lists include the toptables of test statistics and CPM Z-score values for all 18,419 transcripts computed in the analysis. This list excludes lowly expressed and filtered transcripts. All transcripts are expressed as averaged $\log_2$CPM Z-scores.

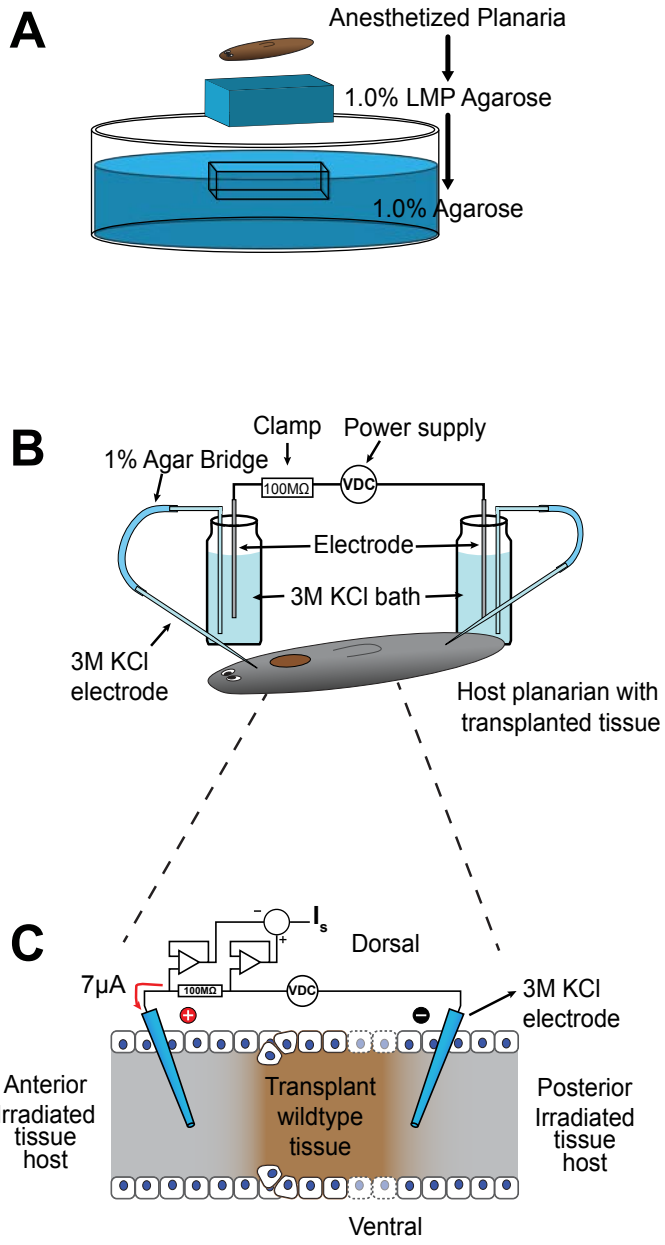

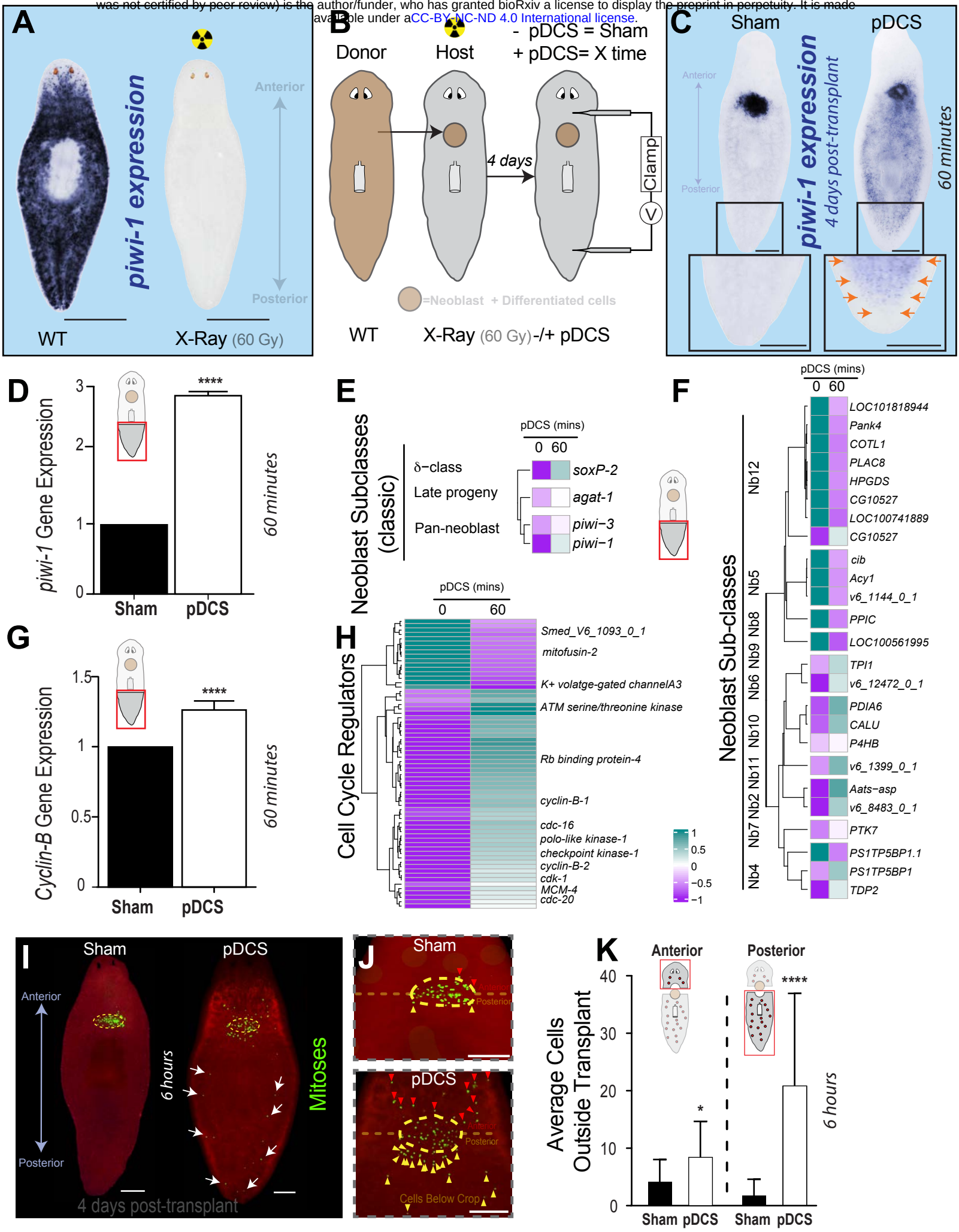

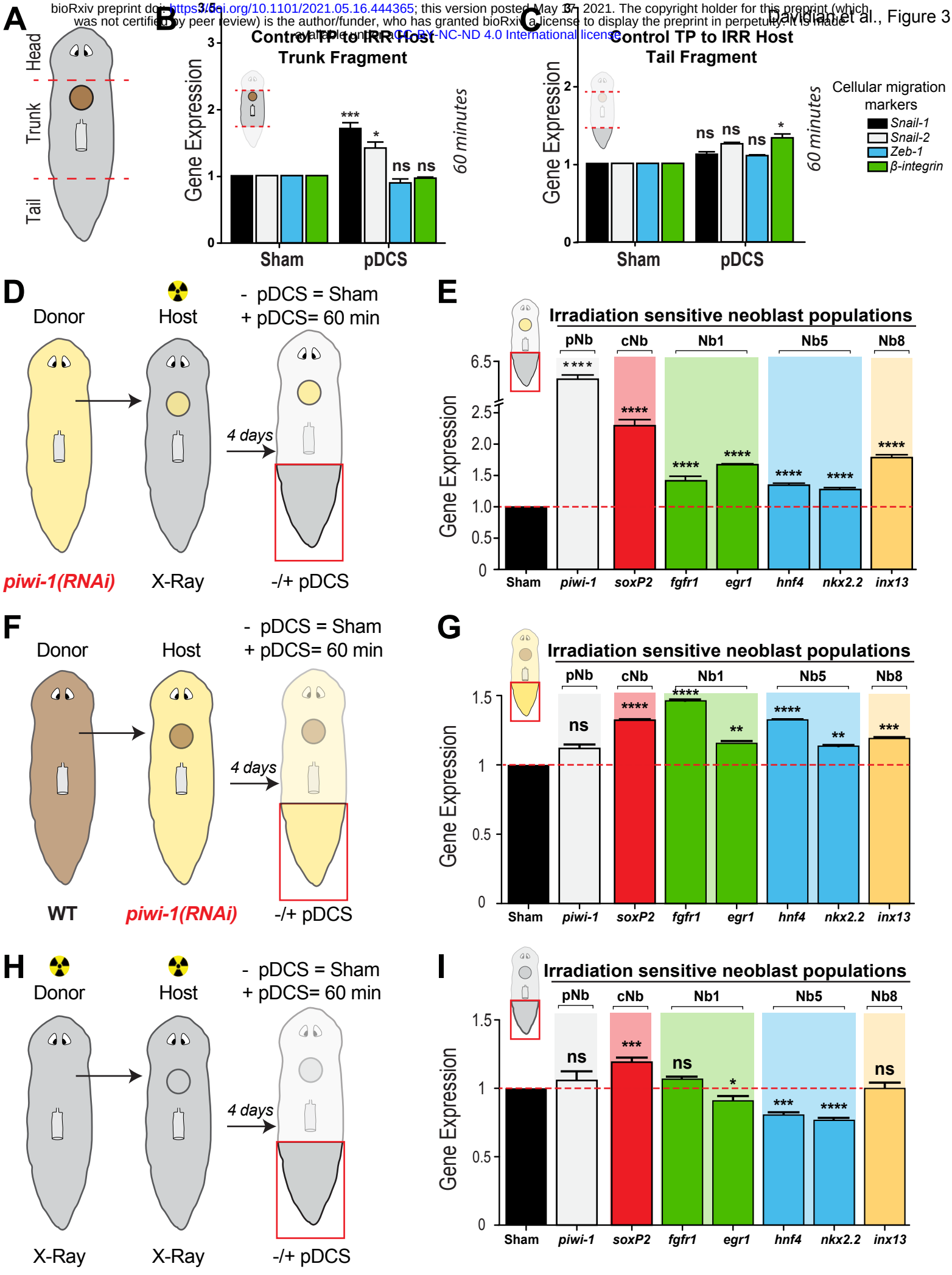

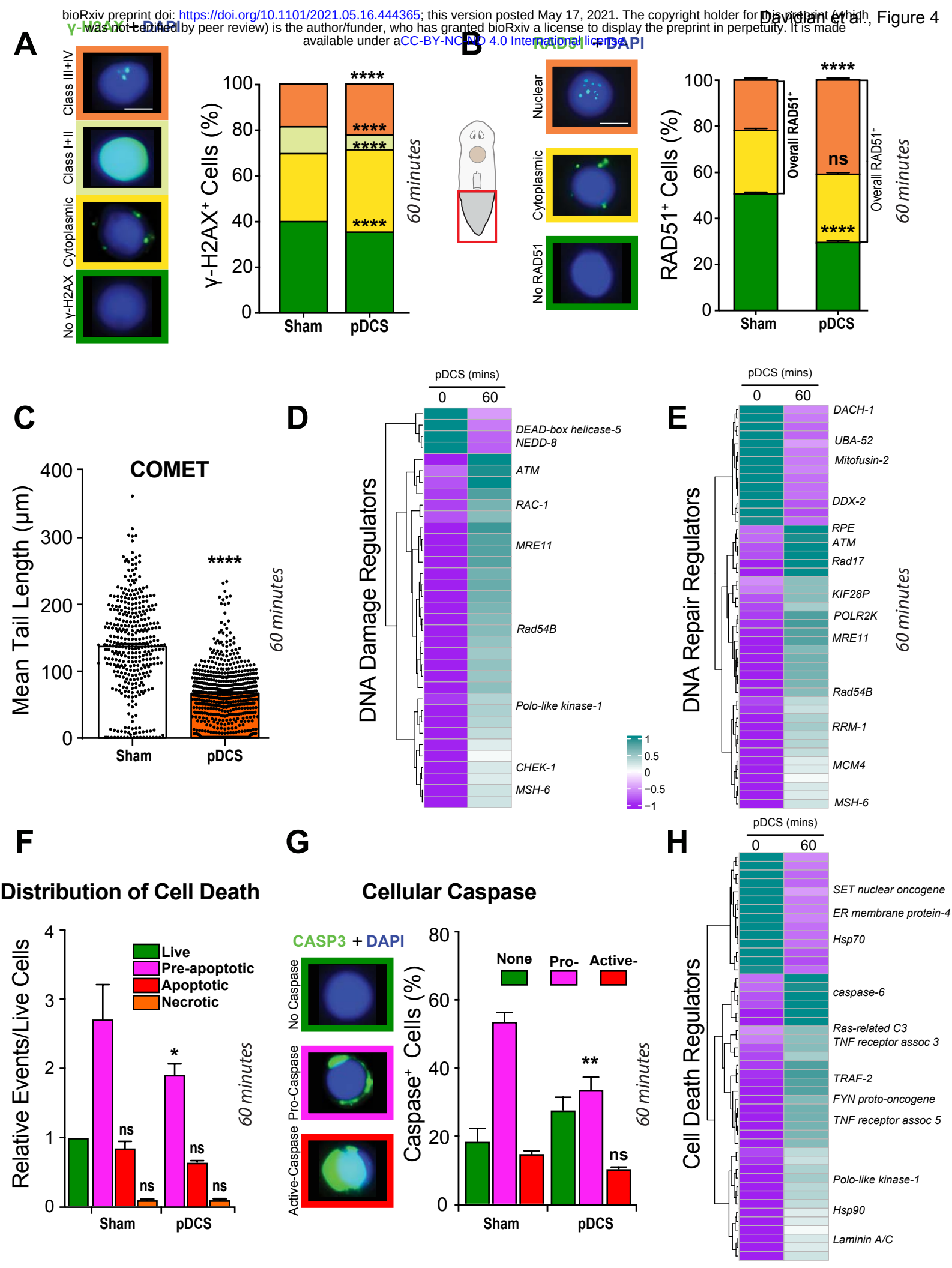

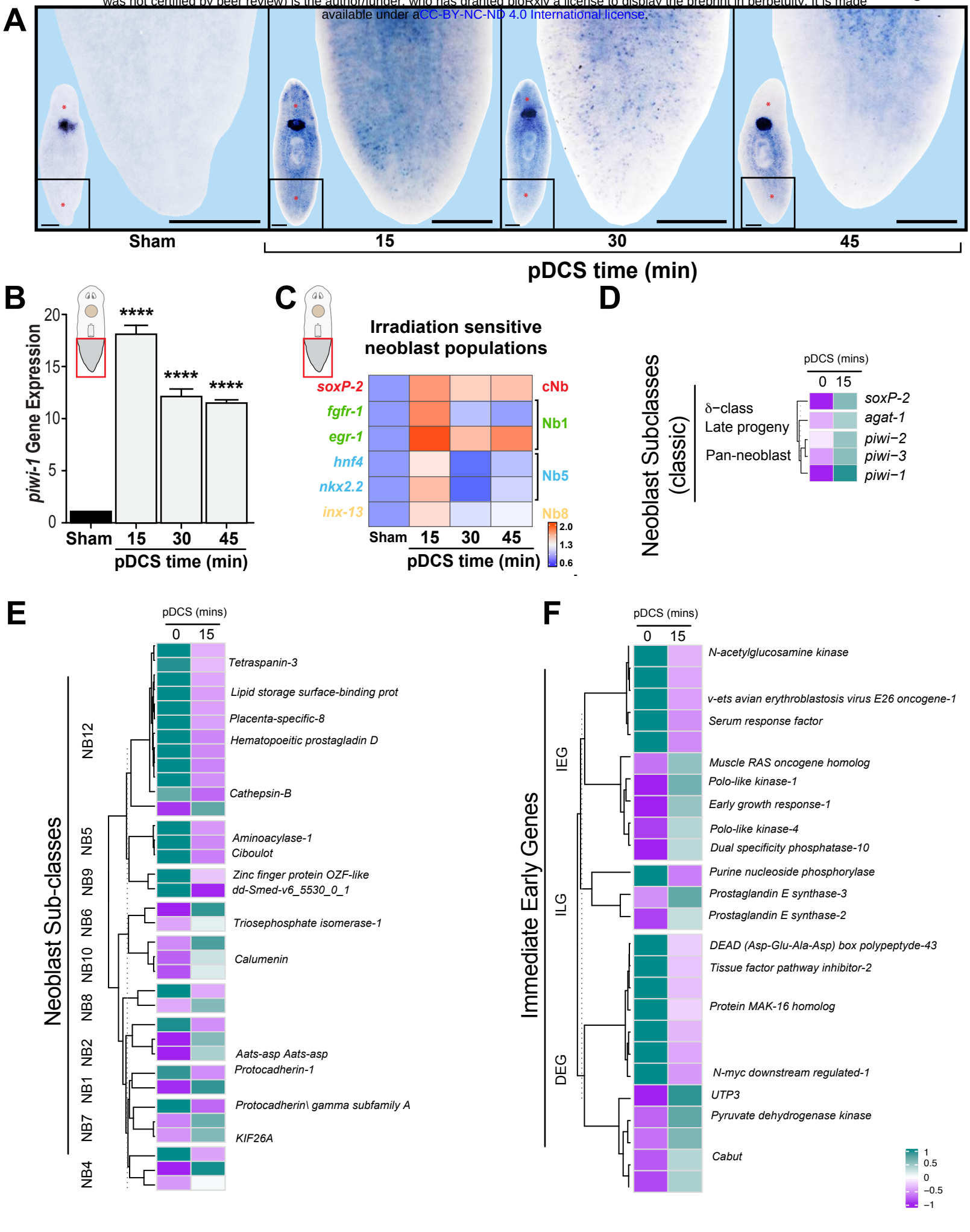

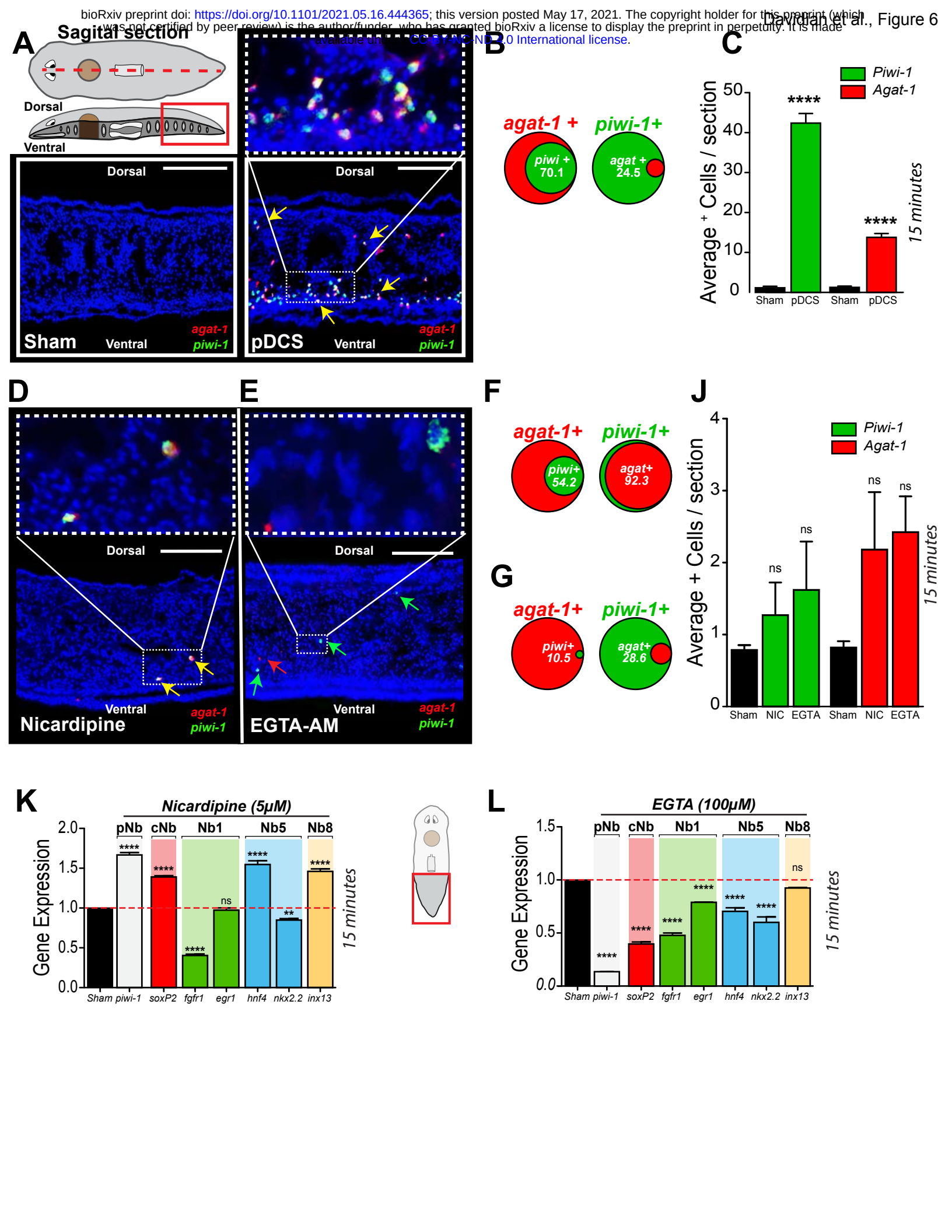

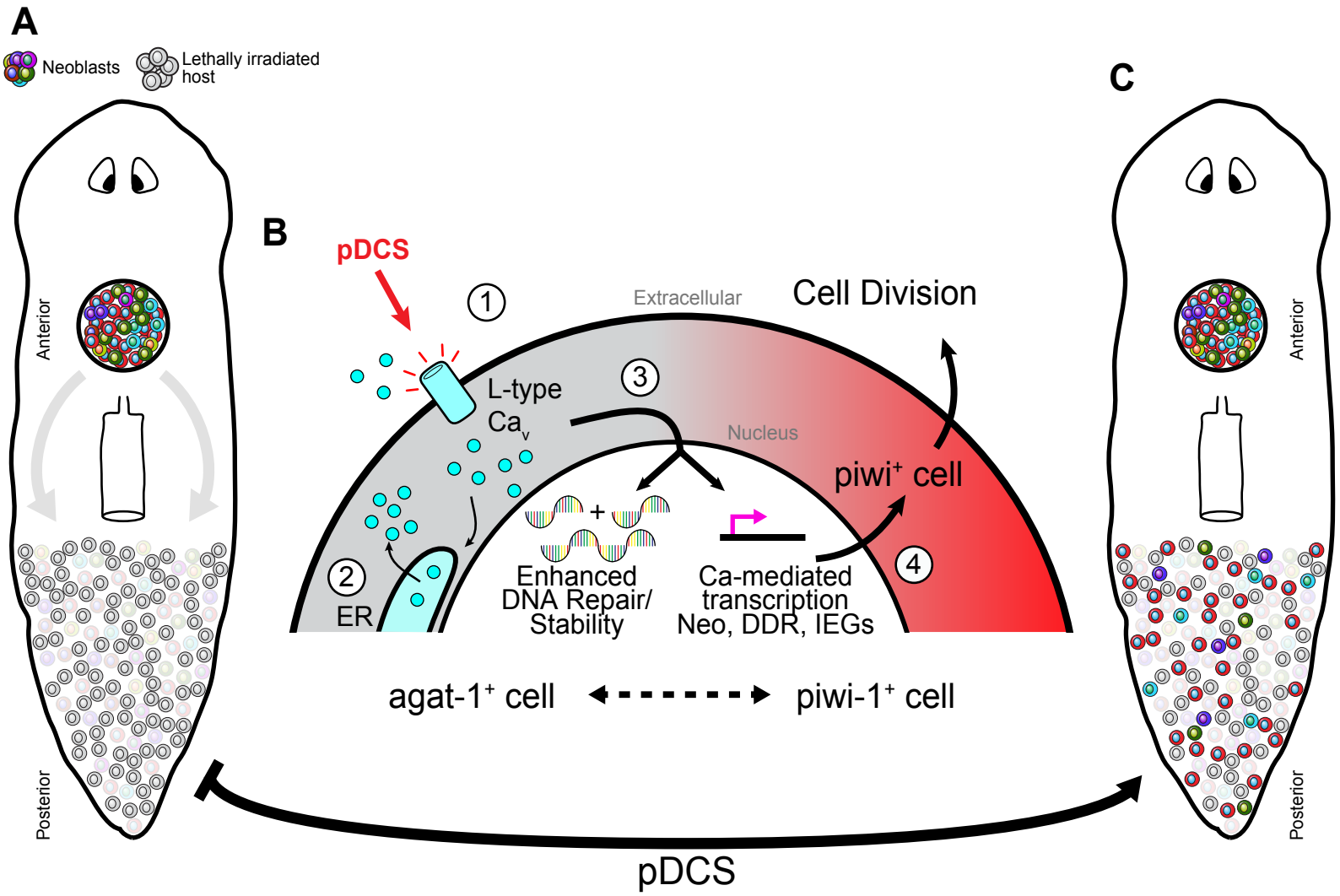

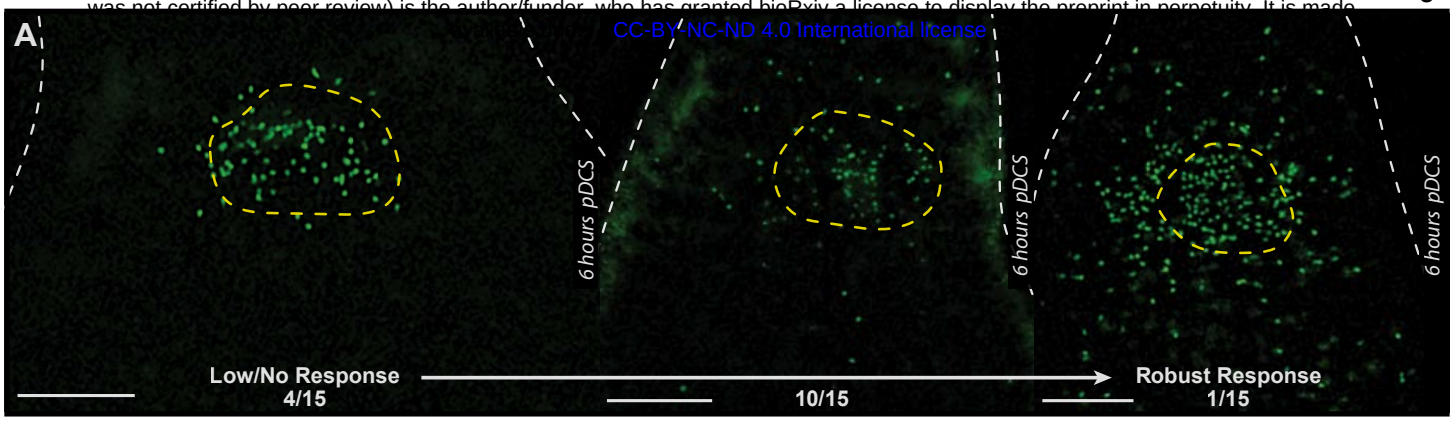

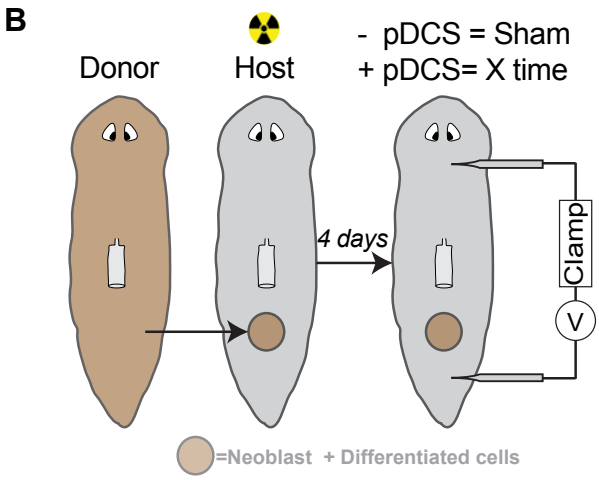

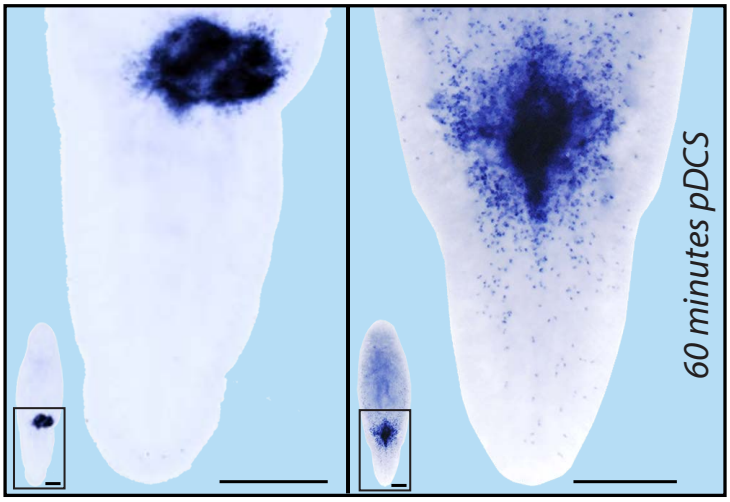

Figure S2

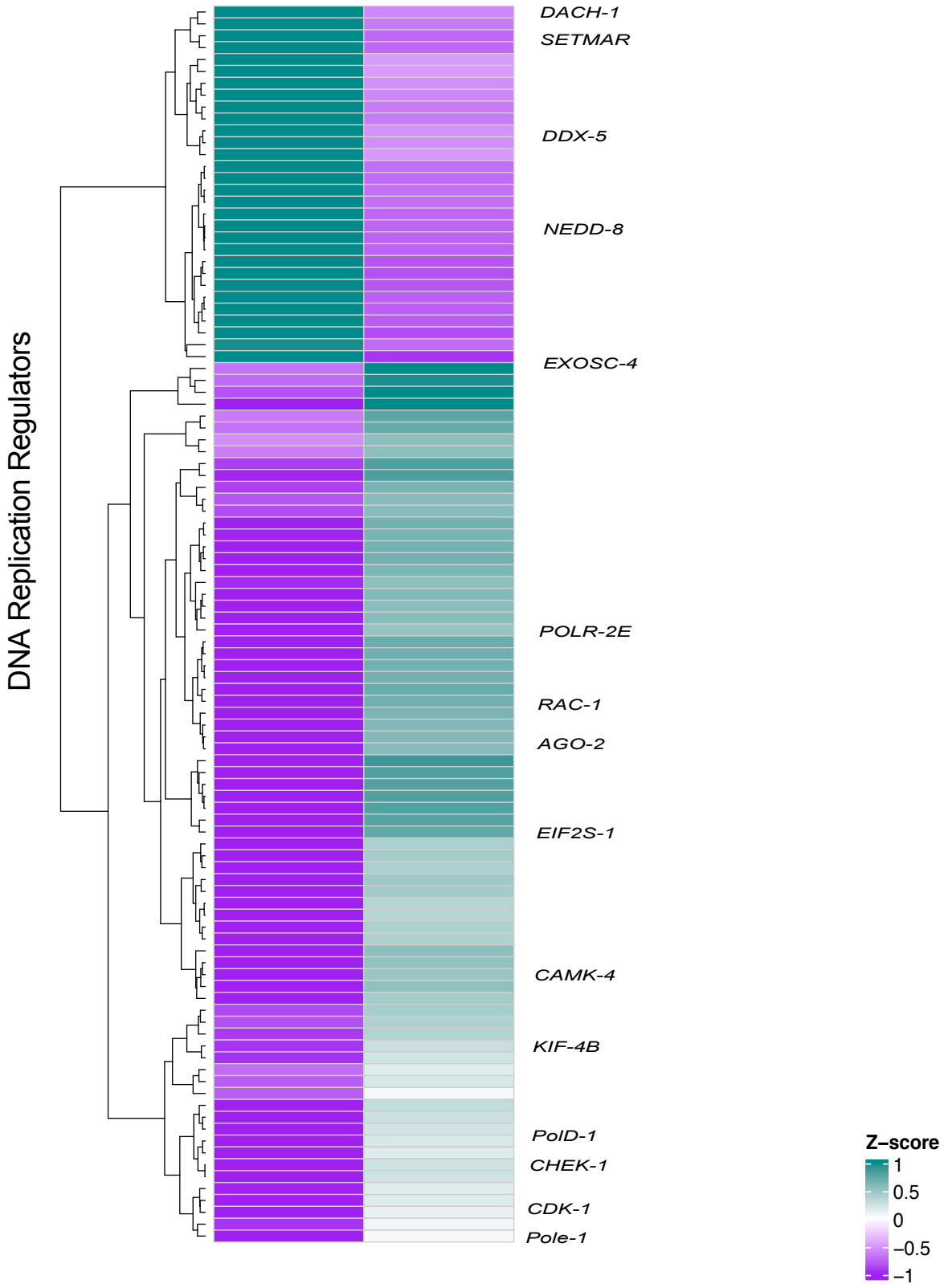

Figure S3

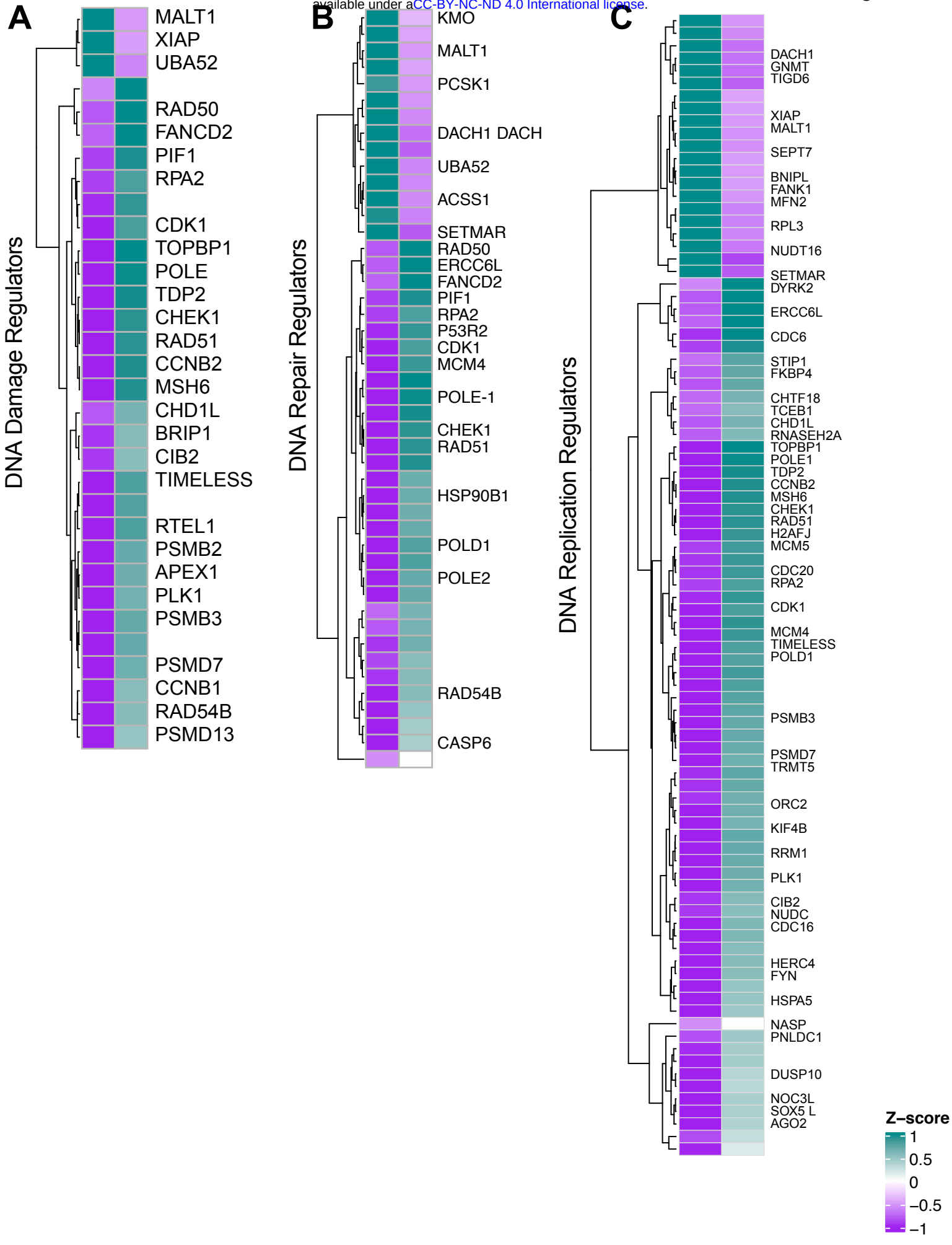

List of Known Immediate Early Genes

Figure S4

Gene Symbol	Gene Name	ENSEMBL ID	Gene Symbol	Gene Name	ENSEMBL ID
JUN	Jun proto-oncogene, AP-1 transcription factor subunit	ENSG00000177606	THBS1	thrombospondin 1	ENSG00000137801
PDK4	**pyruvate dehydrogenase kinase 4**	**ENSG00000004799**	**SRF**	**serum response factor**	**ENSG00000112658**
ZFP36	ZFP36 ring finger protein	ENSG00000128016	ARC	activity regulated cytoskeleton associated protein	ENSG00000198576
HOMER1	homer scaffolding protein 1	ENSG00000152413	ZYX	zyxin	ENSG00000159840
KLF6	Kruppel like factor 6	ENSG00000067082	RNF122	ring finger protein 122	ENSG00000133874
PMM2	phosphomannomutase 2	ENSG00000140650	**NDRG1**	**N-myc downstream regulated 1**	**ENSG00000104419**
DNAJB1(Hsp40 member B1)	DnaJ heat shock protein family	ENSG00000132002	SLC2A3	solute carrier family 2 member 3	ENSG00000059804
GPR50	G protein-coupled receptor 50	ENSG00000102195	**SLC2A1**	**solute carrier family 2 member 1**	**ENSG00000117394**
NXF1	nuclear RNA export factor 1	ENSG00000162231	INSIG1	insulin induced gene 1	ENSG00000186480
JUNB	JunB proto-oncogene, AP-1 transcription factor subunit	ENSG00000171223	RHOB	ras homolog family member B	ENSG00000143878
NR4A3	nuclear receptor subfamily 4 group A member 3	ENSG00000119508	CEBPD	CCAAT/enhancer binding protein delta	ENSG00000221869
GADD45B	growth arrest and DNA damage inducible beta	ENSG00000099860	**PNP**	**purine nucleoside phosphorylase**	**ENSG00000198805**
NR4A2	nuclear receptor subfamily 4 group A member 2	ENSG00000153234	PLAT	plasminogen activator, tissue type	ENSG00000104368
KDM6B	lysine demethylase 6B	ENSG00000132510	TXNL4B	thioredoxin like 4B	ENSG00000140830
F2RL1	F2R like trypsin receptor 1	ENSG00000164251	IER2	immediate early response 2	ENSG00000160888
GTF2B	general transcription factor IIB	ENSG00000137947	PLAU	plasminogen activator, urokinase	ENSG00000122861
F3	coagulation factor III, tissue factor	ENSG00000117525	HAS2	hyaluronan synthase 2	ENSG00000170961
TFB2M	transcription factor B2, mitochondrial	ENSG00000162851	BTG2	BTG anti-proliferation factor 2	ENSG00000159388
UBALD2	UBA like domain containing 2	ENSG00000185262	AKIRIN2	akirin 2	ENSG00000135334
ZFP36L2	ZFP36 ring finger protein like 2	ENSG00000152518	EFNB2	ephrin B2	ENSG00000125266
IER3	immediate early response 3	ENSG00000137331	SYAP1	synapse associated protein 1	ENSG00000169895
PTGS2	**prostaglandin-endoperoxide synthase 2**	**ENSG00000073756**	FOSL1	FOS like 1, AP-1 transcription factor subunit	ENSG00000175592
PPP1R15A	protein phosphatase 1 regulatory subunit 15A	ENSG00000087074	FAM57A	family with sequence similarity 57 member A	ENSG00000167695
SPRY4	sprouty RTK signaling antagonist 4	ENSG00000187678	TNFRSF12A	TNF receptor superfamily member 12A	ENSG00000006327
NPTX2	neuronal pentraxin 2	ENSG00000106236	**PLK2**	**polo like kinase 2**	**ENSG00000145632**
KRT8	keratin 8	ENSG00000170421	CITED2	Cbp/p300 interacting transactivator with Glu/Asp rich carboxy-terminal domain 2	ENSG00000164442
PMAIP1	phorbol-12-myristate-13-acetate-induced protein 1	ENSG00000141682	**TFPI2**	**tissue factor pathway inhibitor 2**	**ENSG00000105825**
KLF10	**Kruppel like factor 10**	**ENSG00000155090**	GEM	GTP binding protein overexpressed in skeletal muscle	ENSG00000164949
YRDC	yrdC N6-threonylcarbamoyltransferase domain containing	ENSG00000196449	C8orf4	chromosome 8 open reading frame 4	ENSG00000176907
CYR61	cysteine rich angiogenic inducer 61	ENSG00000142871	TNFAIP3	TNF alpha induced protein 3	ENSG00000118503
ABHD5	**abhydrolase domain containing 5**	**ENSG00000119798**	SERPINB9	serpin family B member 9	ENSG00000170542
COQ10B	coenzyme Q10B	ENSG00000115520	KLF4	Kruppel like factor 4	ENSG00000136826
MAK16	**MAK16 homolog**	**ENSG00000198042**	MXD1	MAX dimerization protein 1	ENSG00000059728
CTGF	connective tissue growth factor	ENSG00000118523	**RBM14**	**RNA binding motif protein 14**	**ENSG00000239306**
ID4	inhibitor of DNA binding 4, HLH protein	ENSG00000172201	**ETV5**	**ETS variant 5**	**ENSG00000244405**
NFKBIA	NFKB inhibitor alpha	ENSG00000100906	MIDN	midnolin	ENSG00000167470
MYC	v-myc avian myelocytomatosis viral oncogene homolog	ENSG00000136997	PSMD12	proteasome 26S subunit, non-ATPase 12	ENSG00000197170
NIPAL1	NIPA like domain containing 1	ENSG00000163293	EGR2	early growth response 2	ENSG00000122877
FAM83G	family with sequence similarity 83 member G	ENSG00000188522	ZNF26	zinc finger protein 26	ENSG00000198393
BHLHE40	basic helix-loop-helix family member e40	ENSG00000134107	**EGR1**	**early growth response 1**	**ENSG00000120738**
UTP3	**UTP3, small subunit processome component homolog**	**ENSG00000132467**	CA2	carbonic anhydrase 2	ENSG00000104267
TRIB1	**tribbles pseudokinase 1**	**ENSG00000173334**	FOSL2	FOS like 2, AP-1 transcription factor subunit	ENSG00000075426
FLG	filaggrin	ENSG00000143631	FOSB	FosB proto-oncogene, AP-1 transcription factor subunit	ENSG00000125740
DUSP1	dual specificity phosphatase 1	ENSG00000120129	NRARP	NOTCH-regulated ankyrin repeat protein	ENSG00000198435
EREG	epiregulin	ENSG00000124882	KLF2	Kruppel like factor 2	ENSG00000127528
CH25H	cholesterol 25-hydroxylase	ENSG00000138135	CMC2	C-X9-C motif containing 2	ENSG00000103121
ARL5B	ADP ribosylation factor like GTPase 5B	ENSG00000165997	CDKN1A	cyclin dependent kinase inhibitor 1A	ENSG00000124762
GADD45A	growth arrest and DNA damage inducible alpha	ENSG00000116717	CSRNP1	cysteine and serine rich nuclear protein 1	ENSG00000144655
NFKBIZ	NFKB inhibitor zeta	ENSG00000144802	SLC25A25	solute carrier family 25 member 25	ENSG00000148339
NFIL3	nuclear factor, interleukin 3 regulated	ENSG00000165030	ZCCHC12	zinc finger CCHC-type containing 12	ENSG00000174460
DUSP5	**dual specificity phosphatase 5**	**ENSG00000138166**	NPPC	natriuretic peptide C	ENSG00000163273
C6orf141	chromosome 6 open reading frame 141	ENSG00000197261	PHLDA1	pleckstrin homology like domain family A member 1	ENSG00000139289
DUSP6	dual specificity phosphatase 6	ENSG00000139318	SPRY2	sprouty RTK signaling antagonist 2	ENSG00000136158
RND3	Rho family GTPase 3	ENSG00000115963	**RASL11B**	**RAS like family 11 member B**	**ENSG00000128045**
GBP1	guanylate binding protein 1	ENSG00000117228	**NAGK**	**N-acetylglucosamine kinase**	**ENSG00000124357**
QSOX1	quiescin sulfhydryl oxidase 1	ENSG00000116260	EGR4	early growth response 4	ENSG00000135625
LY6K	lymphocyte antigen 6 complex, locus K	ENSG00000160886	EGR3	early growth response 3	ENSG00000179388
ZSWIM6	zinc finger SWIM-type containing 6	ENSG00000130449	RGS2	regulator of G-protein signaling 2	ENSG00000116741
SBDS	SBDS ribosome assembly guanine nucleotide exchange factor	ENSG00000126524	C2orf42	chromosome 2 open reading frame 42	ENSG00000115998
SERPINE1	serpin family E member 1	ENSG00000106366	BAIAP2	BAI1 associated protein 2	ENSG00000175866
MCL1	BCL2 family apoptosis regulator	ENSG00000143384	LIF	leukemia inhibitory factor	ENSG00000128342
GPR3	G protein-coupled receptor 3	ENSG00000181773	NR4A1	nuclear receptor subfamily 4 group A member 1	ENSG00000123358
ERRFI1	ERBB receptor feedback inhibitor 1	ENSG00000116285	ATF3	activating transcription factor 3	ENSG00000162772
MFSD2A	major facilitator superfamily domain containing 2A	ENSG00000168389	ARRDC4	arrestin domain containing 4	ENSG00000140450
SDC4	syndecan 4	ENSG00000124145	BCL10	B-cell CLL/lymphoma 10	ENSG00000142867
HBEGF	heparin binding EGF like growth factor	ENSG00000113070	MAT2A	methionine adenosyltransferase 2A	ENSG00000168906
BCR	BCR, RhoGEF and GTPase activating protein	ENSG00000186716	FOS	Fos proto-oncogene, AP-1 transcription factor subunit	ENSG00000170345
DDX21	**DExD-box helicase 21**	**ENSG00000165732**	IL6	interleukin 6	ENSG00000136244
PSMD12	**proteasome 26S subunit, non-ATPase 12**	**ENSG00000197170**			

Figure S5

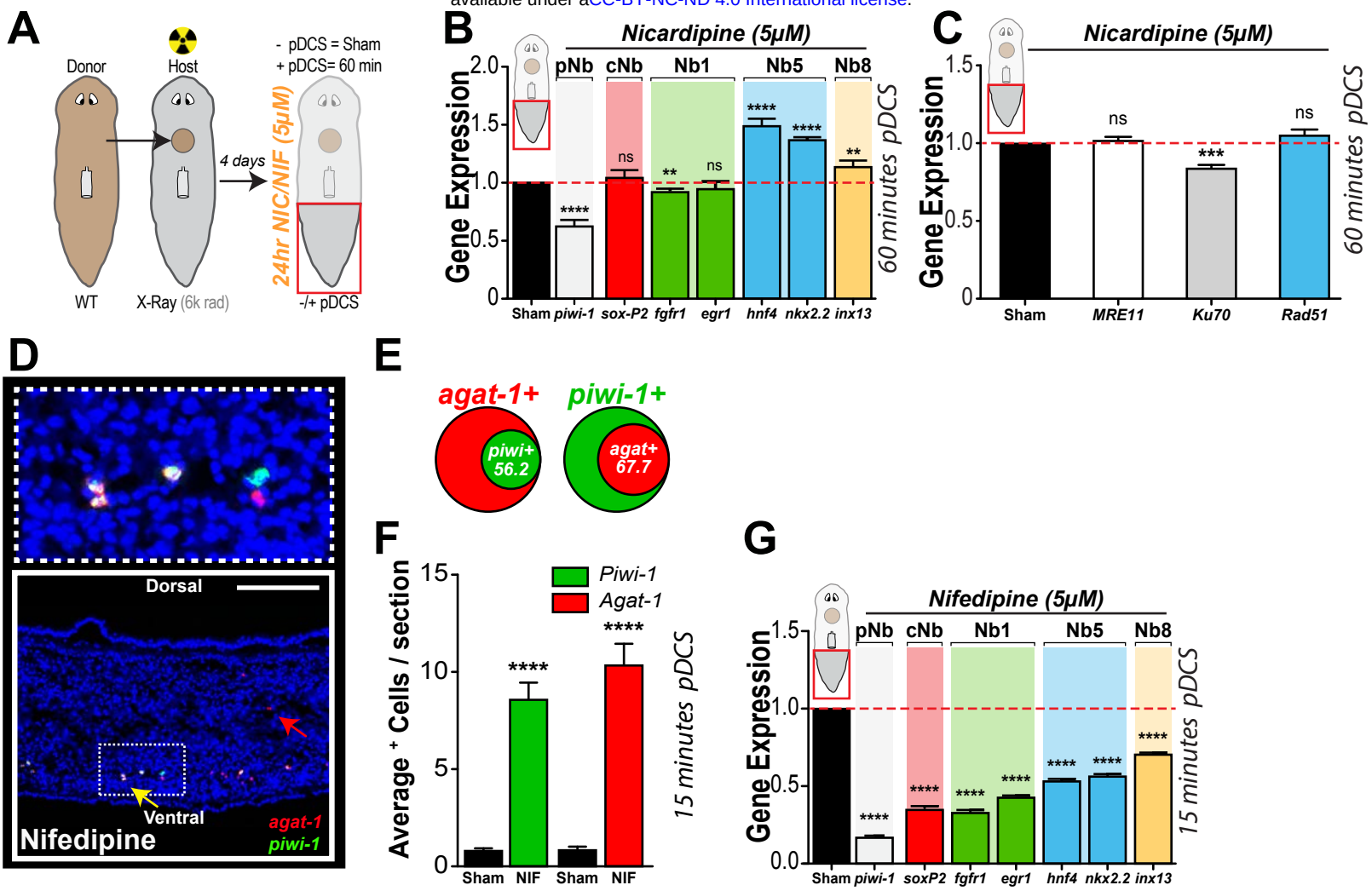

Figure S6

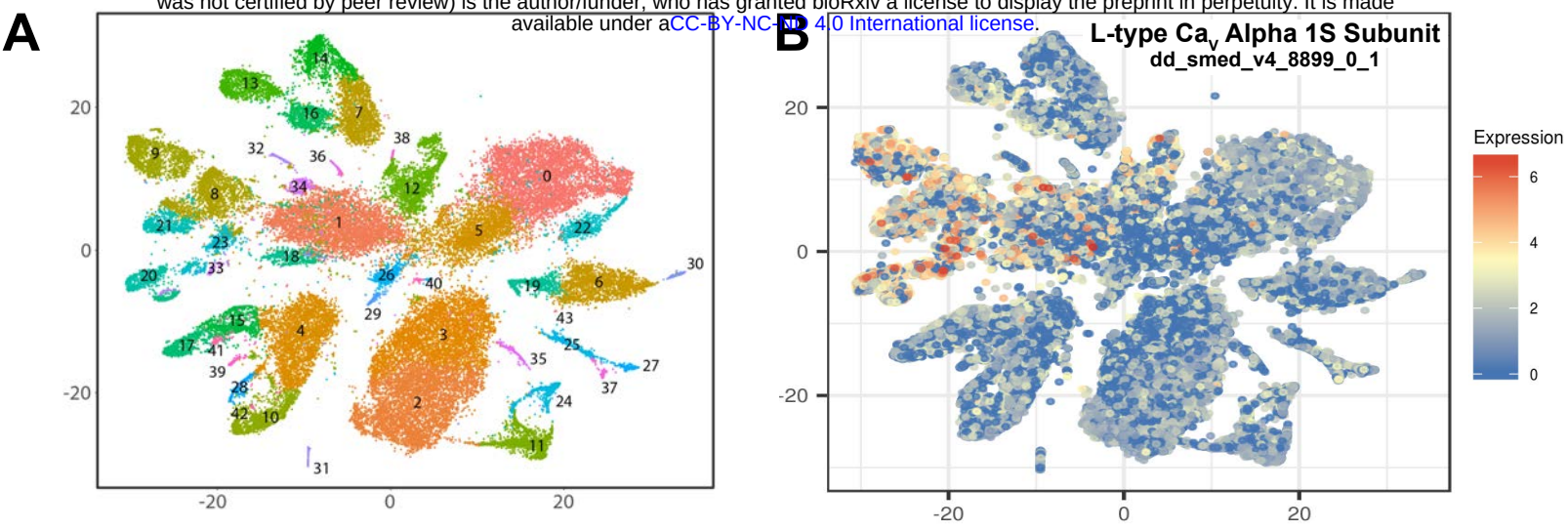

C

Based on main clustering analysis:

Neural: 1, 8, 9, 18, 20, 21, 23, 33, 34; *Parenchymal:* 12, 38

Based on subclustering:

Cathepsin⁺ cells: 8, 10, 15; *Epidermal:* 5, 8, 12
Muscle: 4, 8, 12; *Neural:* 7; *Parenchymal:* 7
Smedwi⁺1 cells: 5, 6, 12, 15